공학박사 학위논문

Interfacial Stabilization of High-Voltage Cathodes in Lithium-Ion Batteries *via* Binder Design

바인더 디자인을 통한
리튬이온전지 고전압 양극재의 계면 안정화

2023 년 2 월

서울대학교 대학원

화학생물공학부

장 바 르 사

Interfacial Stabilization of High-Voltage Cathodes in Lithium-Ion Batteries *via* Binder Design

바인더 디자인을 통한 리튬이온전지 고전압 양극재의 계면 안정화

지도교수 최 장 욱

이 논문을 공학박사 학위논문으로 제출함

2023 년 2 월

서울대학교 대학원
화학생물공학부
장 바 르 사

장바르사의 박사학위논문을 인준함
2023 년 1 월

위 원 장	이 규 태	(인)
부 위 원 장	최 장 욱	(인)
위 원	남 재 욱	(인)
위 원	김 기 재	(인)
위 원	문 준 영	(인)

Abstract

Interfacial Stabilization of High-Voltage Cathodes in Lithium-Ion Batteries *via* Binder Design

Barsa Chang

School of Chemical & Biological Engineering

The Graduate School

Seoul National University

As global warming accelerates in the 21st century, measures to regulate carbon emissions are being actively discussed for sustainable development. In this trend, as the era of full-scale commercialization of electric vehicles begins, lithium-ion batteries (LIBs) and next-generation batteries are receiving tremendous attention. Currently, research is being conducted to increase energy density of the electrode with the goal of improving the mileage, and in the cathode part, high-voltage cathode materials such as layered and spinel structures are considered strong candidates to meet the required demand. However, when the cathode material is driven under a high cut-off voltage condition, the cathode-electrolyte interface (CEI) becomes very unstable, which leads to surface degradation such as electrolyte decomposition. Various attempts have been made to solve this problem, but in this work, the binder, which was mainly considered as an adhesive between the electrode components, was newly provided with the interfacial stabilization function of the high-voltage

cathodes through the multifaceted design of the polymer structure and functional groups. The existing commercial PVDF binder has a relatively weak van der Waals interaction with metal oxide of the cathode. Therefore, the binder coverage on the cathode surface is insufficient so that the naïve cathode surface is easily exposed to the electrolyte. However, in this study, we developed a binder capable of inducing good coverage based on strong interactions such as hydrogen bonding and ion-dipole interaction to alleviate various surface degradations and to form a stable CEI.

In chapter 1, spandex (SPDX) as highly elastic binder is applied for nickel-rich $LiNi_{0.8}Co_{0.1}Mn_{0.1}O_2$ (NCM811) cathodes in LIBs. The nickel-rich layered NCM811 is predominantly used for LIBs intended for electric vehicles owing to their high specific capacities and minimal use of high-cost cobalt. The intrinsic drawbacks of NCM811 with regard to cycle life and safety have largely been addressed by doping with foreign atoms and by applying surface coating. Here, we report that a highly elastic binder, namely SPDX, can overcome the problems of nickel-rich layered cathode materials and improve their electrochemical properties drastically. The high elasticity of spandex allows it to uniformly coat NCM811 particles *via* shear force during slurry mixing to protect the particles from undesired interfacial reactions during cycling. The uniform coating of spandex, together with its hydrogen bonding interaction with metal oxide of NCM811, leads to enhanced particle-to-particle interaction, which has multiple advantages, such as high loading capability, superior rate and cycling performance, and low binder content. This study highlights the promise of elastic binders to meet the ever-challenging criteria with respect to nickel-rich cathode materials in cells targeting electric vehicles.

In chapter 2, λ-carrageenan (CRN) as a sacrificial binder is applied for 5 V $LiNi_{0.5}Mn_{1.5}O_4$ (LNMO) cathodes in LIBs. The spinel LNMO is unique among the cathode materials used in LIBs as it can operate at the highest potential (~4.7 V vs. Li/Li^+). However, high-voltage operation is a double-edged sword for cathodes: good for high energy density but unfavorable for stable cycling. Specifically, the

high-voltage operation in turn decomposes the electrolyte at the CEI, impeding the rate and cycling performance and limiting the widespread industrial adoption of LNMO. This work introduces CRN as a binder for LNMO cathodes to overcome the two challenges these cathodes present during high-voltage operation: cycling stability and high-rate performance. The CRN binder provides good coverage of the LNMO particles via hydrogen and ion-dipole interaction to protect the LNMO surface and thus warrants stable cycling. Moreover, the sulfate group of CRN is decomposed to produce $LiSO_xF$ at the CEI, which supports Li-ion conduction and protects the interface from indiscriminate side reactions of the electrolyte to enhance the rate performance. Thus, the CRN binder is "sacrificial." The concept of a sacrificial binder could be expanded to other emerging electrodes that are detrimentally affected by the oxidative/reductive decomposition of the electrolyte, highlighting the possibility that binders can play a more active role via their chemical functionality.

Keywords : Uniform coverage, Surface degradation, Cathode-electrolyte interface, Polymeric binder, High-voltage cathode, Lithium-ion battery

Student Number : 2018-35512

Contents

List of Tables

List of Figures

Chapter 1. Highly Elastic Binder for $LiNi_{0.8}Co_{0.1}Mn_{0.1}O_2$ Layered Cathodes in Lithium-Ion Batteries

1.1 Introduction

Among the materials being used as cathode materials in lithium-ion batteries (LIBs), nickel (Ni)-rich layered cathode materials are currently receiving the most attention from the battery community.[1] These materials offer multiple attractive features that are beneficial for emerging large-scale LIB applications including electric vehicles (EVs) and grid-scale energy storage systems (ESSs). Ni-rich layered cathode materials have the chemical formulas of either $LiNi_xCo_yMn_zO_2$ or $LiNi_xCo_yAl_zO_2$, where $x+y+z=1$, and are often abbreviated as either NCM*xyz* or NCA*xyz*. The high Ni content is able to increase the specific capacity significantly such that $LiNi_{0.8}Co_{0.1}Mn_{0.1}O_2$ (referred to as NCM811) exhibits a specific capacity of ~200 mAh g^{-1}, which is approximately 40% higher than that of its cobalt (Co)-based counterpart, $LiCoO_2$ (~145 mAh g^{-1}). The origin of this high specific capacity is the small overlap between the e_g band of $Ni^{3+/4+}$ and the $2p$ band of O^{2-},[1a-d] which allows a wider redox range of $Ni^{3+/4+}$ to be employed for Li-ion storage without perturbing the structural stability of the oxygen framework.

Nevertheless, the high Ni content is disadvantageous in that it impairs cycling and adversely affects the thermal stability. Moreover, during synthesis, the chemically unstable Ni^{3+} can be reduced to Ni^{2+}, which can migrate from the transition metal (TM) layer to the Li layer owing to the similar ionic radii[1c-e, 2] of the two cations: Ni^{2+} (0.69 Å) and Li^{+} (0.76 Å). This phenomenon is known[1-3] as cation mixing and causes performance degradation in the key parameters including the cycle life, rate performance, and safety during cycling. Cation mixing induces sequential phase transitions to the spinel and NiO-type rock-salt phases from the surface of each particle. In parallel to these phase transitions, cation mixing leads to

TM dissolution, which triggers[4] unwanted interfacial reactions with the electrolyte *via* catalytic and complexation routes and thus destabilizes the cathode-electrolyte interphase (CEI). These structural and interfacial degradations become significant at elevated temperatures,[5] which explains the inferior cell performance of Ni-rich layered cathode materials at high temperatures. The formation of micro-cracks[6] in the bulk electrode particles is another serious problem associated with Ni-rich layered cathode materials, and impairs the long-term cyclability as a consequence of amplified side reactions with the electrolyte. Thus, the various degradation processes of a Ni-rich layered cathode material are interrelated originating from its intrinsic chemical composition bearing a high content of Ni.

Efforts to mitigate these degradation issues of Ni-rich layered cathode materials have prompted the introduction of a myriad of approaches targeting both the bulk and the surface of the active material. As for modification of the bulk material, the implementation of a Ni concentration gradient[7] such as lowering the Ni content from the core outward is a well-known approach. Doping with foreign atoms[8] was also comprehensively studied because dopants can serve as pillars[8a-c, 8g, 8h, 9] to sustain the lattice framework during cycling. With regard to surface modification, coating with inorganic materials has been widely adopted. These approaches entailing surface coating largely suppress the aforementioned interfacial degradation by way of protecting the active material from the electrolyte.[10] In spite of the considerable positive effects of these bulk- and surface-involved remedies, individual efforts usually result in the limited improvement such that even combined bulk and surface treatments often result in cyclability inferior to that of the established $LiCoO_2$ electrodes.

Motivated to find a solution to the aforementioned problems, we noticed that polymeric binders have rarely been explored for use in Ni-rich layered cathodes even though the binder is a key component of a battery electrode. In particular, we paid attention to elastic binders that had been recently introduced mostly for various

anodes.[11] Elasticity was found to be useful in maintaining the electrode integrity and interface. In the present study, we focus on the elasticity of the polymer as this mechanical property can induce good coverage of the binder over the active particles by utilizing shear force generated during slurry mixing. In the normal procedure of electrode fabrication, which consists of mixing, coating, and drying steps, the spandex (abbreviated as SPDX) elastic binder uniformly covers NCM811 active particles to largely prevent the detrimental interfacial degradation that usually originates from uncontrolled reactions with the electrolyte.[12] Aside from protecting the surfaces of active particles, the SPDX binder permits uniform dispersion of the electrode components and promotes strong electrode adhesion *via* hydrogen bonding interaction between the active particles and the binder. All of these beneficial features of the SPDX binder synergistically improve the cycling and rate performance even at a practically viable binder content of 2 wt%, demonstrating the superiority of this binder to conventional PVDF binders. The present investigation provides a useful lesson in binder design for Ni-rich layered cathode materials by simply focusing on the two properties: elasticity and adhesion.

1.2 Experimental Section

Preparation of Electrode and Cell. The SPDX-based electrode was fabricated by first dispersing commercial NCM811 (L&F Co., D50=10 μm, South Korea), super P (Timcal, Switzerland), and SPDX (TK Chemical, Mw=~213 000, South Korea) in *N*-methyl-2-pyrrolidone (NMP) (Junsei Chemical Co. Ltd., Japan) in a weight ratio of 94:4:2. The slurry was cast onto the Al current collector using the doctor blade method, followed by drying under vacuum at 60 °C overnight. The control PVDF-based electrode was fabricated by using the same procedure except that PVDF (Sigma Aldrich, Mw=~534 000, USA) was used as the binder. The mass loading of the active material was 16.3 mg cm^{-2} for both the PVDF- and SPDX-

based electrodes. For the full-cell tests, the graphite anode was fabricated by first dispersing graphite and the binder consisting of styrene-butadiene rubber (SBR) (Zeon, Japan) and carboxymethyl cellulose (CMC) (Sigma Aldrich, USA) in a weight ratio of 95:5. The weight ratio between SBR and CMC was 1:1. The slurry was cast on the Cu current collector and dried under vacuum at 60 °C overnight. CR2032-coin-type cells were assembled in an Ar-filled glove box. A PE separator (SK Innovation, South Korea) and 1 M $LiPF_6$ in EC/DMC (1/1=v/v) with 10 wt% FEC (PANAX ETEC, South Korea) were used as separator and electrolyte, respectively.

Characterization. The mechanical properties of polymer films were analyzed using a universal testing machine (UTM) (QM100s, QMESYS, South Korea). For this analysis, polymer film specimens were prepared by first drying the polymer solutions at 70 °C overnight and then cutting them with an ASTM D638-Type 5 cutter. 180° peeling tests were conducted to evaluate the adhesive force of each electrode using the same UTM. In this analysis, 3M double-sided tape was attached to each electrode and peeled off at a rate of 25 mm min^{-1}, during which the force was monitored. FT-IR (TEMSOR27, Bruker, Germany) was used to analyze the chemical bonds of the polymers. The surface morphology and binder coverage of the active material were visualized *via* Cs-corrected TEM (JEM-ARM200F, JEOL, Japan) at an acceleration voltage of 80 kV. Top- and cross-sectional images of the electrodes were obtained using field emission-SEM (JSM-7800F Prime, JEOL, Japan) and FIB (Helios 650, FEI, USA). The surface morphology and roughness of the electrodes were characterized using CLSM (LSM 800 MAT, Carl Zeiss, Germany). The amounts of oxygen generated in the half-cells were quantitatively measured using a gas analysis system (HPR-20 R&D, Hiden Analytical, UK). For this analysis, homemade Swagelok-type cells were used, and the oxygen gas from each half-cell was transferred to the gas analysis system *via* a connector through

which Ar gas was flowing at 20 mL min^{-1} after one galvanostatic cycle. Cs-corrected STEM (JEM-ARM200F, JEOL, Japan) was used to visualize the atom-level crystal structures of the samples at an acceleration voltage of 200 kV. The depth profiles of TM and oxygen ions were obtained using ToF-SIMS (TOF.SIMS 5, ION-TOF, Germany). Crystallographic information of the active material was obtained using XRD (SmartLab, Rigaku, Japan) analysis. The degree of TM dissolution was evaluated using EDS elemental mapping (JSM-7800F Prime, JEOL, Japan) and ICP-MS (NexION 350D, Perkin-Elmer, USA). Prior to the ICP-MS analysis, both electrodes were stored in the fresh electrolyte at 60 °C for a different number of days. The surface components of electrodes were characterized using XPS (Axis-Supra, Kratos, UK).

Electrochemical Measurement. Prior to electrochemical tests, all cells were rested for 12 h to enable the electrodes to become sufficiently soaked with the electrolyte. The first two cycles were scanned at 0.1C to induce the formation of a stable CEI layer. Half-cell tests were conducted by adopting galvanostatic charge-discharge mode for each cycle in the potential range of 3.0–4.3 V (*vs.* Li/Li^+) using a battery cycler (WBCS 3000, WonAtech, South Korea). Cyclability tests were performed at 0.5C after the formation cycles mentioned above and rate capability tests were carried out by imposing various C-rates from 0.1C to 2C. During the cyclability tests of the full-cells, constant current constant voltage (CCCV) and constant current (CC) modes were applied for the charging and discharging steps, respectively, in the potential range of 2.8–4.2 V at 0.5C. The electrochemical stability of the polymeric binders was evaluated by conducting cyclic voltammetry (CV) analysis in the potential range of 3.0–4.3 V (*vs.* Li/Li^+) at a scan rate of 0.1 mV s^{-1}. EIS analysis was performed over the frequency range of 0.01 Hz–1 MHz with an amplitude of 10 mV using a potentiostat (VSP, Bio-logic, France).

1.3 Results and Discussion

From the viewpoint of its chemical structure, SPDX generally consists of soft and hard segments (Figure 1a) and these bi-modal segments are responsible for the extraordinary elasticity of SPDX. The soft segments allow the entire polymer matrix to be stretchable while the hard segments mechanically sustain the overall network. The hard segments also account for structural recovery upon release of the stretching force because the recovered polymeric configuration is energetically more favorable.[13] As for the SPDX polymer used in this study, its soft segment is composed of a poly(tetramethylene ether glycol) (PTMEG) unit whereas the hard segment originates from the reaction between methylene diphenyl diisocyanate (MDI) and ethylene diamine (EDA) units (Figure 1a). Notably, the resulting urea and urethane functional groups in the hard segments can participate in hydrogen bonding with the NCM active material (Figure 1b) to induce strong particle-to-particle cohesion and particle-to-current collector adhesion, which is highly critical for high-energy LIBs with high electrode loadings. The molecular structures of the soft and hard segments of the SPDX polymer were investigated by Fourier-transform infrared spectroscopy (FT-IR) analysis (Figure 2a). The soft segments are represented[14] by the strong stretching vibration peak of C–O–C (ether, ~1103 cm^{-1}) whereas the hard segments are identified[13, 15] by the characteristic peaks of –NH– (urethane and urea, ~3325 cm^{-1}), C=O (urethane, ~1731 cm^{-1}), C=O (urea, ~1637 cm^{-1}), and C=C (aromatic, ~1447 cm^{-1}). In addition, the mechanical properties of the PVDF and SPDX binders were compared by characterizing their stress-strain behavior (Figure 1c). The PVDF polymer film ruptured when stretched by only ~15%, whereas the SPDX counterpart sustained elongation even above ~900% owing to its bi-segmental structure. Additionally, a CV test was conducted for both types of polymer electrodes in the potential range of 3.0–4.3 V (*vs.* Li/Li^+) to evaluate their electrochemical stability (Figure 2b and c). Both electrodes exhibited profile shapes consistent with

that of the bare aluminum current collector over the entire potential range, indicating that both polymers have electrochemical stability in the tested potential range.

The extent to which the binder covers the surface of the NCM particles was visualized by conducting transmission electron microscopy (TEM) analysis (Figures 3a–b and 4a–b). In the case of the PVDF-based electrode, the PVDF binder was unevenly distributed and sporadically aggregated on the surface of the NCM particles (Figures 3a and 4a). By contrast, the SPDX binder was clearly observed to be more thinly and uniformly distributed along the surface of the NCM particle (Figures 3b and 4b). The observed SPDX morphology is attributed to the combined effect of its functional groups (Figure 2a) and elasticity (Figure 1c), which results in intimate interaction with the NCM particles throughout the slurry mixing and electrode coating/drying steps. Top-view scanning electron microscopy (SEM) characterization revealed a consistent trend among the electrode components particularly with regard to the conductive agent. The conductive agent was more uniformly distributed in the SPDX-based electrode compared to the PVDF-based electrode (Figures 3c–d and 5a–b). Although the conductive agent is unlikely to undergo chemical interaction with the SPDX, the elasticity of the SPDX binder, together with the higher viscosity of the corresponding slurry (1085.4 cp *vs*. 620.7 cp of the PVDF slurry at a shear rate of 1000.0 s^{-1}) (Figure 6), seemingly induced greater shear stress toward more a uniformly distributed conductive agent.[16] While the uniform coverage of the NCM particles with the binder would be helpful in protecting them from unwanted parasitic reactions, uniform distribution of the conductive agent can facilitate electron transport in the electrode. The distinct distribution of the electrode components was also reflected in the confocal laser scanning microscopy (CLSM) images that map out the surface roughness for an area of 400 × 400 μm^2 (Figure 3e and f). The SPDX electrode showed a smaller range of height deviation over the electrode area compared to that of the PVDF electrode, which is in good agreement with the aforementioned SEM results. The arithmetic

mean roughness values of the two electrodes were 1.9 and 3.1 μm, respectively (Table 1).

Implementation of the SPDX binder also enhanced the mechanical stability of the electrode. Assessment of the electrode adhesion *via* the 180° peeling test using 3M tape (Figure 3g) indicated that the SPDX-based electrode exhibited an adhesion force approximately 10 times as high as that of the PVDF-based electrode on average (1.71 gf mm^{-1} *vs*. 0.17 gf mm^{-1}), reflecting once again the tight NCM-binder interaction *via* hydrogen bonds.[17] The superior adhesion of the SPDX-based electrode was also revealed by cross-sectional SEM analysis (Figure 5c–f). When the electrodes were fabricated under the same conditions (loading of active material = 16.3 mg cm^{-2}), the thickness of the SPDX-based electrode (66.6 μm) was far less than that of the PVDF-based counterpart (109 μm) (Figure 5c and d). In the same context, the stronger adhesion of the SPDX-based electrode to the aluminum current collector was visualized in high-magnification SEM images (Figure 5e and f).

The electrochemical performance of the two electrodes was evaluated in galvanostatic mode by preparing coin-type half-cells. Each electrode consisted of the active material, conductive agent (super P), and binder in a weight ratio of 94:4:2 and the active mass loading was 16.3 mg cm^{-2}. The voltage profiles of both electrodes in their first cycle were almost identical (Figure 7a) such that the operating voltages were near 3.8 V and the reversible capacities were approximately 200 mAh g^{-1}, implying that the SPDX binder did not alter the operating chemistry of the NCM active material. The initial Coulombic efficiencies (ICEs) of the PVDF- and SPDX-based electrodes were 88.8% and 91.4%, respectively, indicating that protection of the surface by the SPDX binder improves the interfacial stability. Gas evolution analysis, furthermore, revealed that the amount of oxygen generated in the SPDX half-cell during the first cycle was smaller than that in the PVDF-based case (1.80 *vs*. 4.45 mL $g_{cathode}^{-1}$) (Figure 8), reconfirming the more stable interface of the SPDX-based electrode during its first (formation) cycle.[18]

When the half-cells were repeatedly cycled in the voltage window of 3.0–4.3 V (*vs*. Li/Li^+) at 0.5C (92.5 mA g^{-1}), the SPDX-based electrode exhibited more sustainable performance compared to that of the PVDF-based electrode (Figure 7b). The PVDF- and SPDX-based electrodes retained 71.6 and 82.5% of their initial capacities after 200 cycles, respectively. The average Coulombic efficiencies (CEs) of both electrodes during 200 cycles were also distinct at 99.74% and 99.92%, respectively. The improved cycling performance of the SPDX-based electrode can be understood by its more stable interface, which benefits from the uniform binder distribution across the NCM particles and the resultant mitigation of undesired reactions with the electrolyte. On the other hand, both electrodes underwent a sudden capacity drop after the 200th cycle due to deterioration of the Li metal counter electrodes upon cycling.

In addition, the SPDX-based electrode exhibited superior rate performance compared with that of the PVDF-based electrode (Figure 7c). When measured at various C-rates from 0.1 to 2C, the SPDX-based binder maintained higher specific capacities and the capacity gap between the two electrodes enlarged as the C-rate increased. For example, at 2C (370 mA g^{-1}), the SPDX- and PVDF-based electrodes retained 129.8 and 100.9 mAh g^{-1}, respectively. In an effort to elucidate the high rate capability of the SPDX-based electrode, electrochemical impedance spectroscopy (EIS) analysis was performed after 50 and 100 cycles (Figure 9a and b). According to the Nyquist plots,[19] both the resistance resulting from the CEI layer (R_2 in the equivalent circuit) and charge-transfer at the active material|electrolyte interface (R_3 in the equivalent circuit) were smaller for the SPDX-based electrode than the PVDF-based electrode. Specifically, the CEI layer-related resistance increased more markedly from the 50th cycle to the 100th cycle for the PVDF-based electrode, indicating the notable difference in the interfacial stability between these two electrodes. In this regard, the more consistent CEI and charge-transfer resistance of the SPDX-based electrode over cycling are attributed to the more uniform coverage

provided by the SPDX binder that contributes to protecting the NCM interface (Figure 3b). On the other hand, the lower charge-transfer resistance of the SPDX-based electrode is related to its compact particle packing as shown in Figure 5c and e. Electrolyte wettability is another factor that has a crucial effect on the accessibility of the electrolyte and the diffusion rate of the Li ion. When the same amount of electrolyte (1 M lithium hexafluorophosphate ($LiPF_6$) in ethylene carbonate (EC)/dimethyl carbonate (DMC) (1/1=*v*/*v*) with 10 wt% fluoroethylene carbonate (FEC) additive) was dropped onto the electrodes, the electrolyte spread out more rapidly over the SPDX-based electrode compared to the PVDF-based electrode (Figure 9c and d). The superior rate performance of the SPDX-based electrode was reflected in its smaller overpotentials at different cycle numbers (Figure 10a).

In an attempt to avoid the effects of Li metal degradation, full-cell tests were conducted by pairing a graphite anode in the voltage range of 2.8–4.2 V at 0.5C (Figure 7d). The cathode mass loading was the same as in the Li half-cell tests (16.3 mg cm^{-2}). The n/p ratios of both cells, defined as the capacity of the anode divided by that of the cathode, were set to 1.1. The SPDX- and PVDF-based full-cells exhibited similar charge-discharge profiles with initial capacities of 189.2 and 183.0 mAh $g_{cathode}^{-1}$ at the 0.1C rate, respectively (Figure 10b). Consistent with the half-cell results, however, the SPDX-based full-cell achieved superior cyclability to that of the PVDF-based full-cell: capacity retention of 96.9% and 80.2% after 250 cycles, respectively. In the same line, the average CE during 250 cycles was higher for the SPDX-based full-cell: 99.82% *vs*. 99.63%. Notably, the CE of the PVDF-based electrode fluctuated more significantly throughout all the cycles, which is consistent with the literature,[20] whereas the CE of the SPDX-based electrode remained stable. On the whole, the SPDX binder was proven to be effective in extending the cycle life of Ni-rich NCM electrodes in both half-cell and full-cell settings.

Ni-rich NCM materials are well known to adversely experience internal micro-crack formation along the grain boundaries, which arises from the repeated

anisotropic volume change associated with the H2→H3 phase transition at around 4.15 V *vs*. Li/Li^+.[6d, 21] As the micro-cracks propagate through secondary particles, electrolyte penetration becomes a serious problem in that it promotes the growth of the CEI layer to ultimately increase the interfacial resistance.[6] The extent of micro-crack generation was compared in the cross-sectional SEM images (Figure 11) after dissecting the electrodes using the focused ion beam (FIB) technique. According to this analysis, micro-crack formation was clearly more severe in the PVDF-based electrode (Figure 11a and c) compared with the SPDX-based electrode (Figure 11b and d). Two possible explanations exist for the lessened micro-crack formation of the SPDX-based electrode; first, micro-crack formation can be seen to be triggered by structural degradation of the particle surface. Degradation of the surface structure as the result of TM dissolution and layered-to-spinel phase transitions and the continued propagation of these two phenomena into the particle interior accelerate the formation of micro-cracks. Thus, the uniform and tight coverage of the active particles by the SPDX binder can mitigate micro-crack formation. Second, the high elasticity of the SPDX binder exerts a counter-force against the volume expansion of the active particle, thereby distributing the stress during volume change.[11e-g] For reference, the stress in an object can evolve into cracks when the stress is released without a counter-balancing force. Although understanding the detailed mechanism thereof would require an additional in-depth investigation, the distinct levels of micro-crack formation between both electrodes were reproducibly observed in multiple samples and are thus worth taking as a reflection of the actual impact of the binder. In correspondence with the electrochemical performance in Figure 7, the lessened micro-crack formation in the SPDX-based electrode is largely responsible for its superior cyclability.

In the highly delithiated state, the TM ions in the NCM material tend to migrate from the TM layers to the lithium layers (unoccupied lithium sites). This migration results in a structural transformation from the rhombohedral layered phase

($R\bar{3}m$) to the spinel ($Fd\bar{3}m$) phase and then to the rock-salt ($Fm\bar{3}m$) phase by engaging in cation mixing.[22] These phase transitions could be accelerated in highly delithiated states by TM dissolution caused by hydrofluoric acid (HF) attack. These structural alterations weaken the interfacial stability by triggering parasitic reactions, which harms the cyclability of the corresponding cell. In this line, the effect of the SPDX binder on maintaining the structure was investigated by scanning transmission electron microscopy (STEM) analysis in high-angle annular dark-field (HAADF) mode (Figure 12). In the pristine state, both the PVDF- and SPDX-based electrodes exhibited only a limited cation-mixed layer (~1.5 nm deep) (Figure 12a and b) which was formed during synthesis of the material. However, the depth of the phase transition became significantly different for the two electrodes after 100 cycles. While the original layered structure was substantially transformed into the spinel and rock-salt phases (~4 and ~3 nm thick, respectively) in the PVDF-based electrode (Figure 12c), the layered structure of the SPDX-based electrode remained dominant with the depth of the spinel phase remaining less than ~2.5 nm (Figure 12d). This phase information was further verified by fast Fourier-transform (FFT) analyses (Figure 12e and f), which were conducted for the white-dotted boxes in Figure 12c and d. The series of FFT patterns reconfirm the more advanced penetration of the PVDF-based electrode by the spinel and rock-salt phases.

The X-ray diffraction (XRD) patterns of both electrodes (Figure 13a and b) revealed consistent results in terms of the level of cation mixing. In these analyses, the levels of cation mixing were estimated *via* the intensity ratio between the (003) and (104) peaks.[23] In the pristine state, the ratios were similar at 1.11 and 1.07 for the PVDF- and SPDX-based electrodes, respectively. However, these values decreased distinctly to 0.78 and 1.02, respectively, after 100 cycles, reflecting more significant cation mixing and thus phase degradation of the PVDF-based electrode. Hence, the uniform coating of the SPDX binder was quite effective in preserving the structure of the NCM811 material, and is also linked to the interfacial stability.

It has long been known that divalent TM ions are liable to dissolution in the carbonate electrolyte as a result of attack by HF,[4a, 4c-f] which is inevitably present because of the reaction between $LiPF_6$ and trace amounts of water. In an attempt to determine the effect of protecting the surface of the SPDX binder, both electrodes were subjected to inductively coupled plasma-mass spectrometry (ICP-MS) analysis after 250 cycles. In preparation for this analysis, after cycling, both the PVDF- and SPDX-based electrodes were stored in fresh electrolyte (1 M $LiPF_6$ in EC/DMC (1/1=*v*/*v*) with 10 wt% FEC additive) at 60 °C for different periods. Remarkably, the SPDX-based electrode clearly exhibited less dissolution of all three the TM ions that were tested compared to those of the PVDF-based electrode for all the storage periods (Table 2). For the same purpose, namely to assess TM dissolution, the polyethylene (PE) separators were analyzed by energy dispersive spectroscopy (EDS) elemental mapping after 250 cycles. Consistent with the above ICP-MS results, lower signals were detected for the separator of the SPDX-based full-cell with respect to all three the TM ions (Figure 14a and b). As TM dissolution is known to trigger undesired side reactions at the interfaces of both sides of a cell, the diminished TM dissolution resulting from SPDX coverage is largely responsible for the observed improved cyclability of the SPDX-based cells.

Layered metal oxides in the delithiated state are highly reactive such that the organic electrolyte in contact can be oxidatively decomposed to form a CEI layer on the surface of the electrode. In the case of common carbonate electrolytes that contain $LiPF_6$, it is accepted that the CEI layer consists of two parts: the inner and outer layers.[5a, 24] The inner layer is mainly composed of LiF, fluoroorganic compounds, and corroded NCM, whereas the main components of the outer layer are $Li_xPO_yF_z$ and aliphatic moieties. X-ray photoelectron spectroscopy (XPS) analysis was employed to elucidate the components of the CEI layers or those near the surfaces of the electrodes (Figure 15). The F 1s spectra (Figure 15a and b) of both of the electrodes in the pristine state confirmed the bond identities of the

corresponding binders. However, the two electrodes exhibited different trends after 100 cycles. The emergence of LiF and $Li_xPO_yF_z$ peaks (~685.5 eV and ~687.0 eV, respectively) in the PVDF-based electrode was more prominent[25] unlike its SPDX-based counterpart, which is attributed to more significant exposure of the electrode to the electrolyte that leads to increased interfacial reactions. With respect to the Ni 2p spectra (Figure 15c and d), the two electrodes showed different traits even in the pristine state. While the profile of the SPDX-based electrode was almost feature-less, the PVDF-based electrode exhibited NiO peaks at ~854.8 eV and $Ni(OH)_2$ peaks at ~856.7 eV. The silent profile of the SPDX-based electrode reflects the effective coverage of the binder. After 100 cycles, the NiO peaks could scarcely be observed for the PVDF-based electrode (Figure 15c) because the active material was buried beneath the CEI layer. Instead, NiF_2,[5a] which precipitated from the electrolyte, was newly detected as a result of TM dissolution. The profile of the SPDX-based electrode remained feature-less. On the other hand, the distinct TM dissolution was detected by conducting a depth profile analysis using time-of-flight secondary ion mass spectrometry (ToF-SIMS) with respect to various ions (Ni, Co, Mn, O) (Figure 16). In the pristine state, when analyzed as a function of increasing sputtering time, both the PVDF- and SPDX-based electrodes exhibited almost depth-independent profiles with respect to the three TM ions (Figure 16a and b). Thus, the effect of the binder was invisible. By contrast, after 100 cycles, the intensity profiles of the TM ions initially revealed steep slopes during sputtering of both electrodes (Figure 16c and d). The sloping behavior results from the formation of the CEI layer on the electrode surface. Notably, the duration of this sloping region was clearly longer for the PVDF-based electrode than for the SPDX-based electrode, which reflects the thicker CEI layer on the PVDF-based electrode. Interestingly, in the case of the PVDF electrode (Figure 16c), the extent to which the intensity of the Mn profile decreases toward the electrode surface is more prominent compared to those of the other two TMs as well as that of the Mn profile in the SPDX-based electrode (Figure

16d). This observation points to the fact that Mn is more vulnerable[4a, 4c, 4d, 26] to dissolution than the other TMs and that the SPDX binder is able to effectively protect the surface by suppressing Mn dissolution.

1.4 Conclusion

This study uncovers a promising opportunity with regard to advanced binder design to improve the key electrochemical properties of Ni-rich layered cathode materials. These materials are currently making major advances toward extending the driving distance of electric vehicles and lowering the battery cost represented by the dollar-per-kilowatt metric. The high elasticity and strong adhesion of the SPDX binder enable it to uniformly cover NCM particles with minimal content by utilizing the shear force exerted while the slurry is being mixed. The uniform and conformal coverage by the binder protects the surface of the NCM particles from unwanted TM dissolution and parasitic reactions to improve the cycle life markedly. The use of SPDX as the binder also greatly mitigates the formation of micro-cracks, another seriously problematic phenomenon arising from increased Ni content. This study unveils "elasticity and adhesion" as the key features to pursue when designing future binders intended for use with even higher Ni content such as >90 at.%.

1.5 Reference

[1] a) A. Manthiram, J. C. Knight, S.-T. Myung, S.-M. Oh, Y.-K. Sun, *Adv. Energy Mater.* **2016**, 6, 1501010; b) J. Xu, F. Lin, M. M. Doeff, W. Tong, *J. Mater. Chem. A* **2017**, 5, 874; c) W. Li, B. Song, A. Manthiram, *Chem. Soc. Rev.* **2017**, 46, 3006; d) W. Liu, P. Oh, X. Liu, M.-J. Lee, W. Cho, S. Chae, Y. Kim, J. Cho, *Angew. Chem. Int. Ed.* **2015**, 54, 4440; e) S.-T. Myung, F. Maglia, K.-J. Park, C. S. Yoon, P. Lamp, S.-J. Kim, Y.-K. Sun, *Acs Energy*

Lett. **2016**, 2, 196.

[2] a) J. Zhao, W. Zhang, A. Huq, S. T. Misture, B. Zhang, S. Guo, L. Wu, Y. Zhu, Z. Chen, K. Amine, F. Pan, J. Bai, F. Wang, *Adv. Energy Mater.* **2017**, 7, 1601266; b) F. Wu, J. Tian, Y. Su, J. Wang, C. Zhang, L. Bao, T. He, J. Li, S. Chen, *ACS Appl. Mater. Interfaces* **2015**, 7, 7702.

[3] a) Y. S. Meng, G. Ceder, C. P. Grey, W.-S. Yoon, M. Jiang, J. Breger, Y. Shao-Hom, *Chem. Mater.* **2005**, 17, 2386; b) X. Zhang, W. J. Jiang, A. Mauger, Qilu, F. Gendron, C. M. Julien, *J. Power Sources* **2010**, 195, 1292.

[4] a) H. Zheng, Q. Sun, G. Liu, X. Song, V. S. Battaglia, *J. Power Sources* **2012**, 207, 134; b) Z. Q. Deng, A. Manthiram, *J. Phys. Chem. C* **2011**, 115, 7097; c) R. Jung, F. Linsenmann, R. Thomas, J. Wandt, S. Solchenbach, F. Maglia, C. Stinner, M. Tromp, H. A. Gasteiger, *J. Electrochem. Soc.* **2019**, 166, A378; d) M. Evertz, F. Horsthemke, J. Kasnatscheew, M. Börner, M. Winter, S. Nowak, *J. Power Sources* **2016**, 329, 364; e) T. Deng, X. Fan, L. Cao, J. Chen, S. Hou, X. Ji, L. Chen, S. Li, X. Zhou, E. Hu, D. Su, X.-Q. Yang, C. Wang, *Joule* **2019**, 3, 2550; f) D.-S. Ko, J.-H. Park, S. Park, Y. N. Ham, S. J. Ahn, J.-H. Park, H. N. Han, E. Lee, W. S. Jeon, C. Jung, *Nano Energy* **2019**, 56, 434.

[5] a) D. Li, H. Li, D. Danilov, L. Gao, J. Zhou, R.-A. Eichel, Y. Yang, P. H. L. Notten, *J. Power Sources* **2018**, 396, 444; b) K. Edström, T. Gustafsson, J. O. Thomas, *Electrochim. Acta* **2004**, 50, 397; c) D. Aurbach, *J. Power Sources* **2003**, 119-121, 497.

[6] a) S. Watanabe, M. Kinoshita, T. Hosokawa, K. Morigaki, K. Nakura, *J. Power Sources* **2014**, 258, 210; b) J.-M. Lim, T. Hwang, D. Kim, M.-S. Park, K. Cho, M. Cho, *Sci. Rep.* **2017**, 7, 39669; c) K. Ishidzu, Y. Oka, T. Nakamura, *Solid State Ionics* **2016**, 288, 176; d) H.-H. Ryu, K.-J. Park, C.

S. Yoon, Y.-K. Sun, *Chem. Mater.* **2018**, 30, 1155.

[7] a) Y.-K. Sun, S.-T. Myung, B.-C. Park, J. Prakash, I. Belharouak, K. Amine, *Nat. Mater.* **2009**, 8, 320; b) Y.-K. Sun, S.-T. Myung, M.-H. Kim, J. Prakash, K. Amine, *J. Am. Chem. Soc.* **2005**, 127, 13411; c) J.-Y. Liao, A. Manthiram, *J. Power Sources* **2015**, 282, 429; d) X. Xu, L. Xiang, L. Wang, J. Jian, C. Du, X. He, H. Huo, X. Cheng, G. Yin, *J. Mater. Chem. A* **2019**, 7, 7728; e) P. Hou, X. Wang, D. Wang, D. Song, X. Shi, L. Zhang, J. Guo, J. Zhang, *RSC Adv.* **2014**, 4, 15923; f) P. Y. Hou, L. Q. Zhang, X. P. Gao, *J. Mater. Chem. A* **2014**, 2, 17130.

[8] a) W. Hua, J. Zhang, Z. Zheng, W. Liu, X. Peng, X.-D. Guo, B. Zhong, Y.-J. Wang, X. Wang, *Dalton Trans.* **2014**, 43, 14824; b) Z. Huang, Z. Wang, Q. Jing, H. Guo, X. Li, Z. Yang, *Electrochim. Acta* **2016**, 192, 120; c) F. Schipper, M. Dixit, D. Kovacheva, M. Talianker, O. Haik, J. Grinblat, E. M. Erickson, C. Ghanty, D. T. Major, B. Markovsky, D. Aurbach, *J. Mater. Chem. A* **2016**, 4, 16073; d) X. Li, K. Zhang, M. Wang, Y. Liu, M. Qu, W. Zhao, J. Zheng, *Sustainable Energy Fuels* **2018**, 2, 413; e) F. Dogan, J. T. Vaughey, H. Iddir, B. Key, *ACS Appl. Mater. Interfaces* **2016**, 8, 16708; f) Y.-C. Li, W. Xiang, Z.-G. Wu, C.-L. Xu, Y.-D. Xu, Y. Xiao, Z.-G. Yang, C.-J. Wu, G.-P. Lv, X.-D. Guo, *Electrochim. Acta* **2018**, 291, 84; g) M. Chen, E. Zhao, D. Chen, M. Wu, S. Han, Q. Huang, L. Yang, X. Xiao, Z. Hu, *Inorg. Chem.* **2017**, 56, 8355; h) W. Cho, Y. J. Lim, S.-M. Lee, J. H. Kim, J.-H. Song, J.-S. Yu, Y.-J. Kim, M.-S. Park, *ACS Appl. Mater. Interfaces* **2018**, 10, 38915; i) J. Zheng, W. H. Kan, A. Manthiram, *ACS Appl. Mater. Interfaces* **2015**, 7, 6926.

[9] a) H. Li, P. Zhou, F. Liu, H. Li, F. Cheng, J. Chen, *Chem. Sci.* **2019**, 10, 1374; b) H. Yang, H.-H. Wu, M. Ge, L. Li, Y. Yuan, Q. Yao, J. Chen, L. Xia, J. Zheng, Z. Chen, J. Duan, K. Kisslinger, X. C. Zeng, W.-K. Lee, Q. Zhang,

J. Lu, *Adv. Funct. Mater.* **2019**, 29, 1808825.

[10] a) G. Hu, Y. Tao, Y. Lu, J. Fan, L. Li, J. Xia, Y. Huang, Z. Zhang, H. Su, Y. Cao, *ChemElectroChem* **2019**, 6, 4773; b) K. Du, H. Xie, G. Hu, Z. Peng, Y. Cao, F. Yu, *ACS Appl. Mater. Interfaces* **2016**, 8, 17713; c) A. M. Wise, C. Ban, J. N. Weker, S. Misra, A. S. Cavanagh, Z. Wu, Z. Li, M. S. Whittingham, K. Xu, S. M. George, M. F. Toney, *Chem. Mater.* **2015**, 27, 6146; d) J. Wang, C. Du, C. Yan, X. He, B. Song, G. Yin, P. Zuo, X. Cheng, *Electrochim. Acta* **2015**, 174, 1185; e) J.-Z. Kong, S.-S. Wang, G.-A. Tai, L. Zhu, L.-G. Wang, H.-F. Zhai, D. Wu, A.-D. Li, H. Li, *J. Alloys Compd.* **2016**, 657, 593; f) F. Schipper, H. Bouzaglo, M. Dixit, E. M. Erickson, T. Weigel, M. Talianker, J. Grinblat, L. Burstein, M. Schmidt, J. Lampert, C. Erk, B. Markovsky, D. T. Major, D. Aurbach, *Adv. Energy Mater.* **2018**, 8, 1701682; g) T. Tao, C. Chen, Y. Yao, B. Liang, S. Lu, Y. Chen, *Ceram. Int.* **2017**, 43, 15173; h) S.-U. Woo, C. S. Yoon, K. Amine, I. Belharouak, Y.-K. Sun, *J. Electrochem. Soc.* **2007**, 154; i) R. Zhao, J. Liang, J. Huang, R. Zeng, J. Zhang, H. Chen, G. Shi, *J. Alloys Compd.* **2017**, 724, 1109; j) W. Liu, M. Wang, X. l. Gao, W. Zhang, J. Chen, H. Zhou, X. Zhang, *J. Alloys Compd.* **2012**, 543, 181.

[11] a) X. Zhu, F. Zhang, L. Zhang, L. Zhang, Y. Song, T. Jiang, S. Sayed, C. Lu, X. Wang, J. Sun, Z. Liu, *Adv. Funct. Mater.* **2018**, 28, 1705015; b) C. Milroy, A. Manthiram, *Adv. Mater.* **2016**, 28, 9744; c) L. Wang, T. Liu, X. Peng, W. Zeng, Z. Jin, W. Tian, B. Gao, Y. Zhou, P. K. Chu, K. Huo, *Adv. Funct. Mater.* **2018**, 28, 1704858; d) D.-J. Yoo, A. Elabd, S. Choi, Y. Cho, J. Kim, S. J. Lee, S. H. Choi, T.-w. Kwon, K. Char, K. J. Kim, A. Coskun, J. W. Choi, *Adv. Mater.* **2019**, 31, 1901645; e) Z. Xu, J. Yang, T. Zhang, Y. Nuli, J. Wang, S.-i. Hirano, *Joule* **2018**, 2, 950; f) S. Choi, T.-W. Kwon, A. Coskun, J. W. Choi, *Science* **2017**, 357, 279; g) Y. Cho, J. Kim, A. Elabd, S. Choi, K. Park, T.-W. Kwon, J. Lee, K. Char, A. Coskun, J. W. Choi, *Adv. Mater.* **2019**, 31, 1905048.

[12] a) L. Zheng, H. Zhang, P. Cheng, Q. Ma, J. Liu, J. Nie, W. Feng, Z. Zhou, *Electrochim. Acta* **2016**, 196, 169; b) S. Zhang, H. Gu, H. Pan, S. Yang, W. Du, X. Li, M. Gao, Y. Liu, M. Zhu, L. Ouyang, D. Jian, F. Pan, *Adv. Energy Mater.* **2016**, 7, 1601066.

[13] K. Zhang, A. M. Nelson, S. J. Talley, M. Chen, E. Margaretta, A. G. Hudson, R. B. Moore, T. E. Long, *Green Chem.* **2016**, 18, 4667.

[14] N. Iqbal, P. K. Sharma, D. Kumar, P. K. Roy, *Constr. Build. Mater.* **2018**, 175, 682.

[15] A. Tcharkhtchi, S. Farzaneh, S. Abdallah-Elhirtsi, B. Esmaeillou, F. Nony, A. Baron, *Int. J. Polym. Anal. Ch.* **2014**, 19, 571

[16] V. Collin, I. Boudimbou, E. Peuvrel-Disdier, *J. Appl. Polym. Sci.* **2013**, 127, 2121.

[17] P. K. Forooshani, B. P. Lee, *J. Polym. Sci. A Polym. Chem.* **2017**, 55, 9.

[18] a) R. Jung, M. Metzger, F. Maglia, C. Stinner, H. A. Gasteiger, *J. Electrochem. Soc.* **2017**, 164, A1361; b) C. S. Johnson, J.-S. Kim, C. Lefief, N. Li, J. T. Vaughey, M. M. Thackeray, *Electrochem. Commun.* **2004**, 6, 1085.

[19] a) M. Wang, R. Zhang, Y. Gong, Y. Su, D. Xiang, L. Chen, Y. Chen, M. Luo, M. Chu, *Solid State Ionics* **2017**, 312, 53; b) Q. Fan, S. Yang, J. Liu, H. Liu, K. Lin, R. Liu, C. Hong, L. Liu, Y. Chen, K. An, P. Liu, Z. Shi, Y. Yang, *J. Power Sources* **2019**, 421, 91.

[20] J. Kim, H. Ma, H. Cha, H. Lee, J. Sung, M. Seo, P. Oh, M. Park, J. Cho, *Energy Environ. Sci.* **2018**, 11, 1449.

[21] a) J. Yang, Y. Xia, *ACS Appl. Mater. Interfaces* **2016**, 8, 1297; b) F. Wu, N. Liu, L. Chen, Y. Su, G. Tan, L. Bao, Q. Zhang, Y. Lu, J. Wang, S. Chen, J.

Tan, *Nano Energy* **2019**, 59, 50; c) H. Li, A. Liu, N. Zhang, Y. Wang, S. Yin, H. Wu, J. R. Dahn, *Chem. Mater.* **2019**, 31, 7574.

[22] a) S.-K. Jung, H. Gwon, J. Hong, K.-Y. Park, D.-H. Seo, H. Kim, J. Hyun, W. Yang, K. Kang, *Adv. Energy Mater.* **2014**, 4, 1300787; b) H. H. Li, N. Yabuuchi, Y. S. Meng, S. Kumar, J. Breger, C. P. Grey, Y. Shao-Horn, *Chem. Mater.* **2007**, 19, 2551; c) F. Lin, I. M. Markus, D. Nordlund, T.-C. Weng, M. D. Asta, H. L. Xin, M. M. Doeff, *Nat. Commun.* **2014**, 5, 3529.

[23] a) H. Arai, S. Okada, H. Ohtsuka, M. Ichimura, J. Yamaki, *Solid State Ionics* **1995**, 80, 261; b) I. H. Son, J. H. Park, S. Kwon, J. Mun, J. W. Choi, *Chem. Mater.* **2015**, 27, 7370.

[24] a) N. Schulz, R. Hausbrand, C. Wittich, L. Dimesso, W. Jaegermann, *J. Electrochem. Soc.* **2018**, 165, A833; b) Q.-Q. Ren, F.-D. Yu, S.-W. Zhang, B.-S. Yin, Z.-B. Wang, K. Ke, *Electrochim. Acta* **2019**, 297, 1011.

[25] a) X. Fan, L. Chen, X. Ji, T. Deng, S. Hou, J. Chen, J. Zheng, F. Wang, J. Jiang, K. Xu, C. Wang, *Chem* **2018**, 4, 174; b) B. Ziv, V. Borgel, D. Aurbach, J.-H. Kim, X. Xiao, B. R. Powell, *J. Electrochem. Soc.* **2014**, 161, A1672.

[26] C. Zhan, T. Wu, J. Lu, K. Amine, *Energy Environ. Sci.* **2018**, 11, 243.

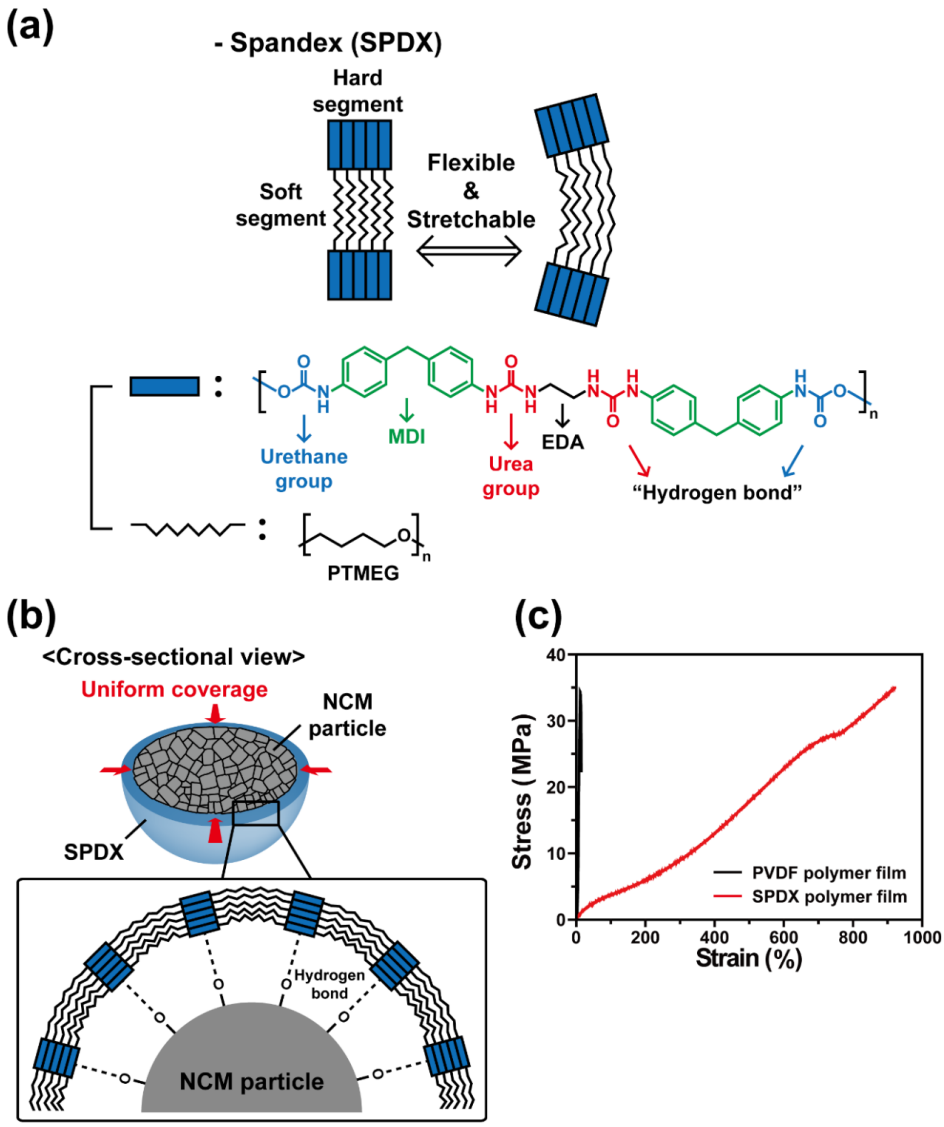

Figure 1.1. (a) Graphical representation of the SPDX binder and its chemical structure. (b) Binding scheme of the SPDX binder with NCM particle *via* hydrogen bonding interaction. (c) Stress-strain curves of the PVDF and SPDX polymer films.

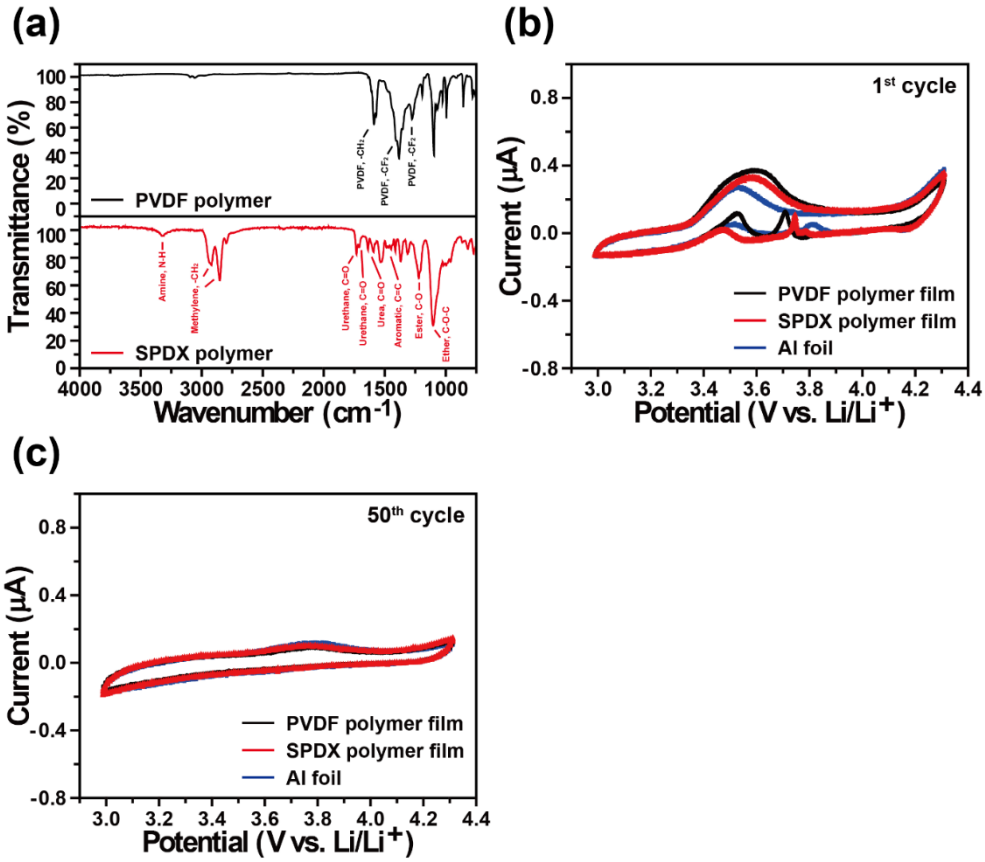

Figure 1.2. (a) FT-IR spectra of the PVDF and SPDX polymer films. CV curves of the PVDF polymer film, SPDX polymer film, and Al current collector at a scan rate of 0.1 mV s^{-1} at the (b) 1st cycle and (c) 50th cycle.

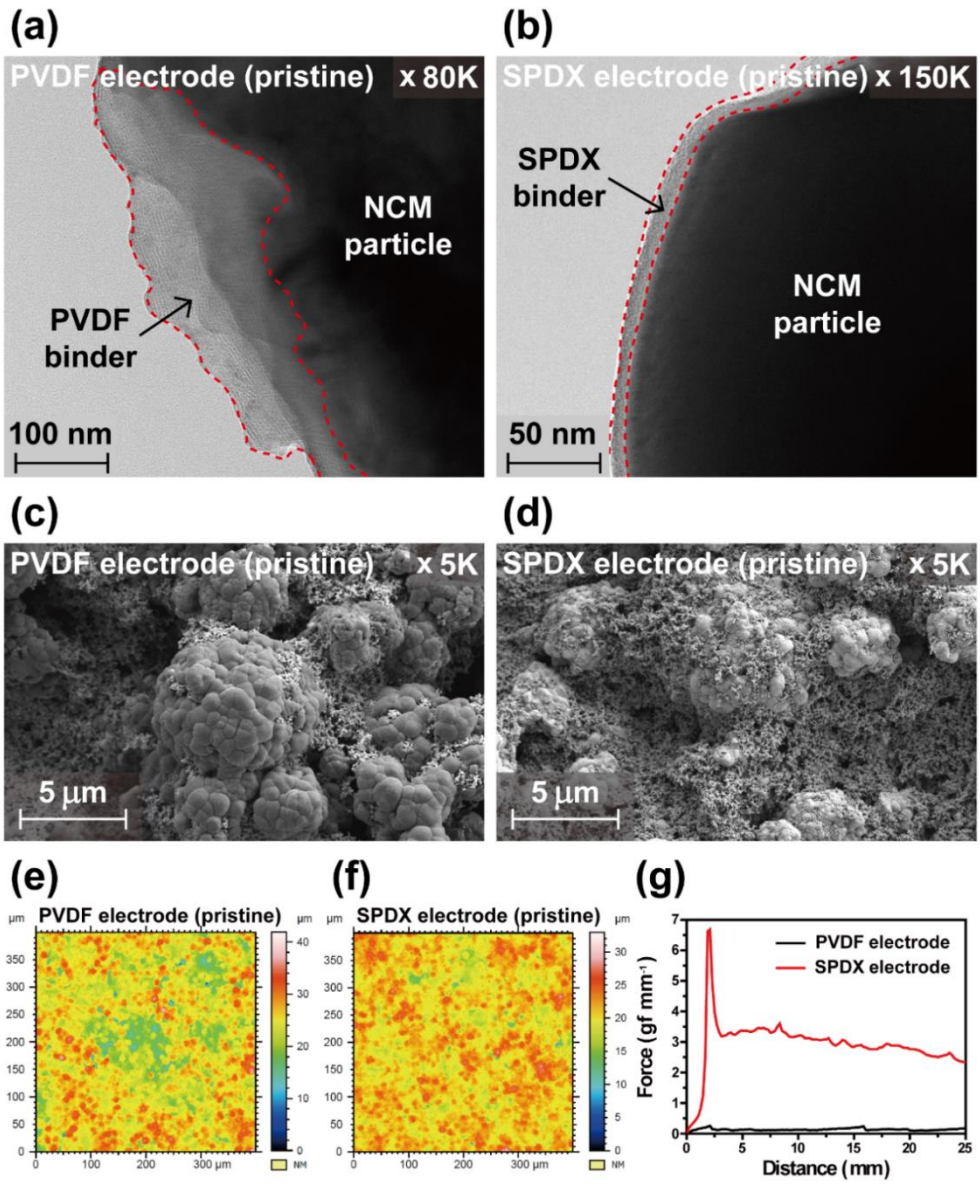

Figure 1.3. Elasticity of the SPDX binder for uniform coverage of an NCM particle. TEM images of the (a) PVDF and (b) SPDX binders on an NCM particle in the pristine state. The red dotted lines indicate the boundaries of the binder coverage. High-magnification top-view SEM images of the (c) PVDF- and (d) SPDX-based electrodes. CLSM surface topography images of the (e) PVDF- and (f) SPDX-based electrodes in the pristine state. (g) 180° peeling test curves of the PVDF- and SPDX-based electrodes.

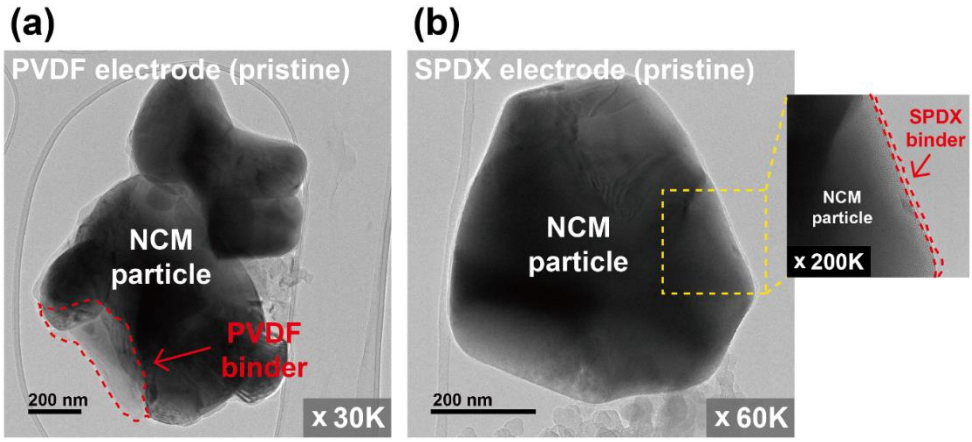

Figure 1.4. Low-magnification TEM images of the (a) PVDF and (b) SPDX binders on an NCM particle in the pristine state.

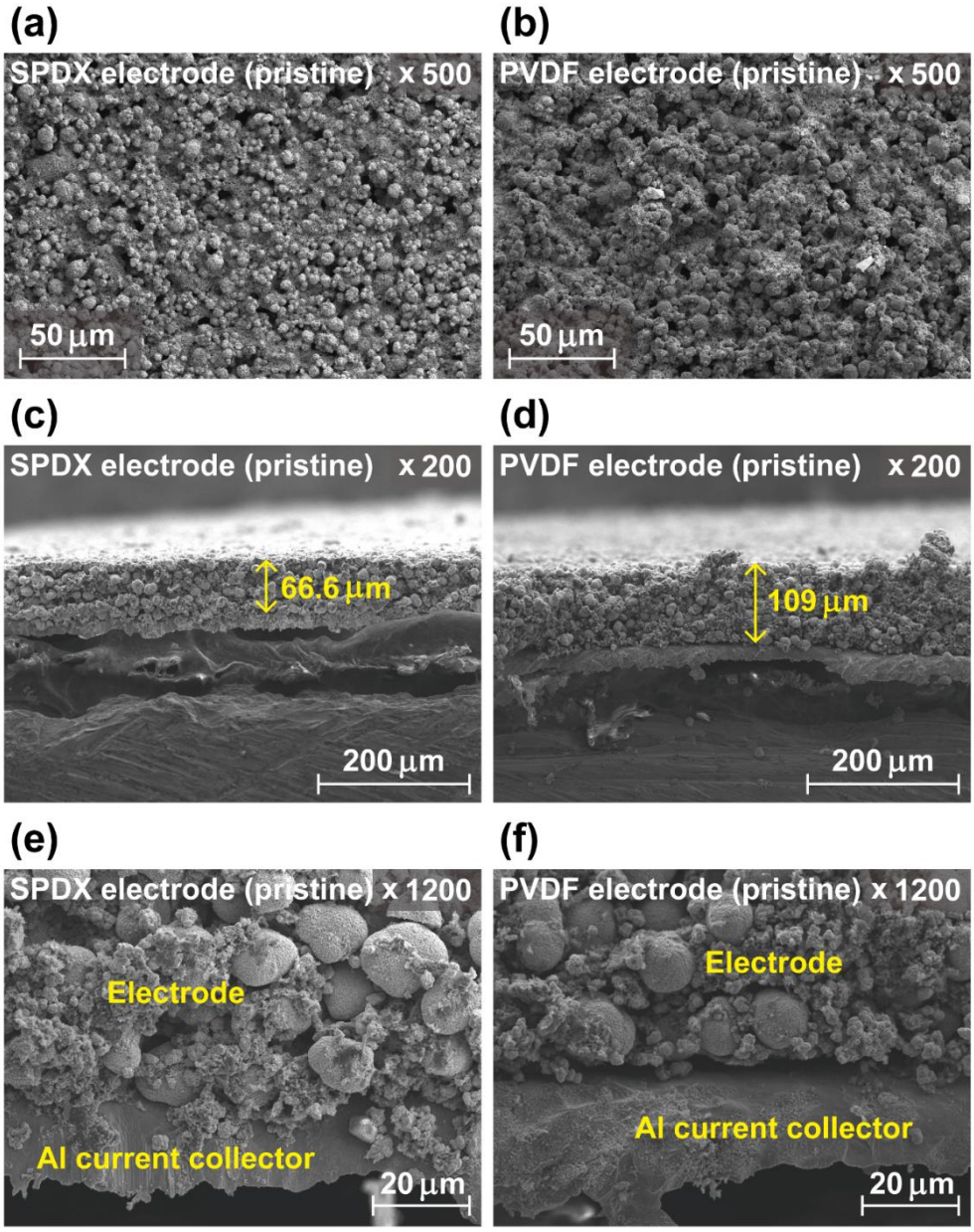

Figure 1.5. Top-view SEM images of the (a) SPDX- and (b) PVDF-based electrodes in the pristine state. Cross-sectional SEM images of the (c) SPDX- and (d) PVDF-based electrodes in the pristine state. High-magnification cross-sectional SEM images of the (e) SPDX- and (f) PVDF-based electrodes in the pristine state.

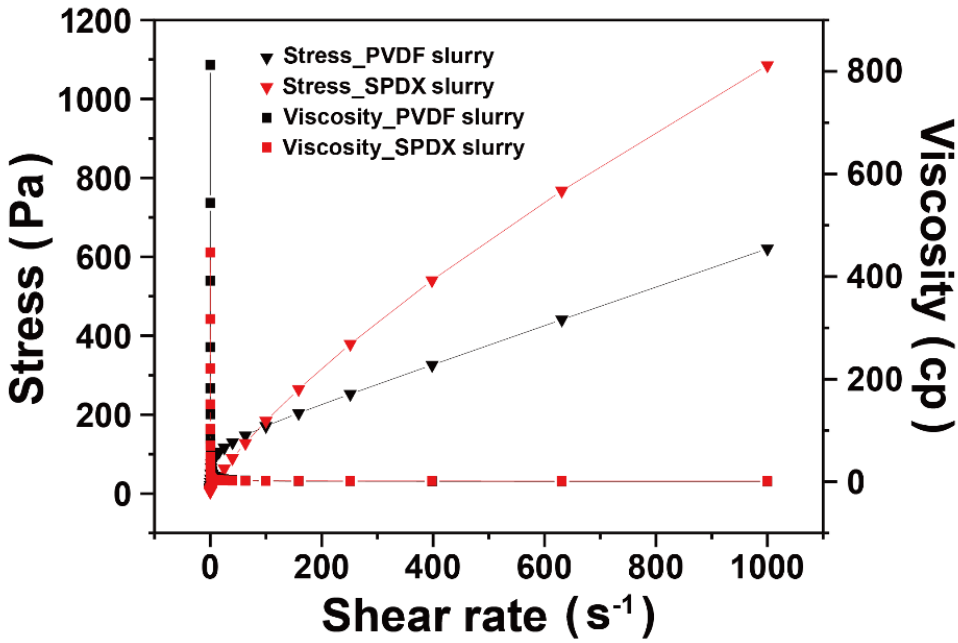

Figure 1.6. Rheological data of the PVDF- and SPDX-based electrode slurries prepared with the same contents of active material, conductive agent, and binder.

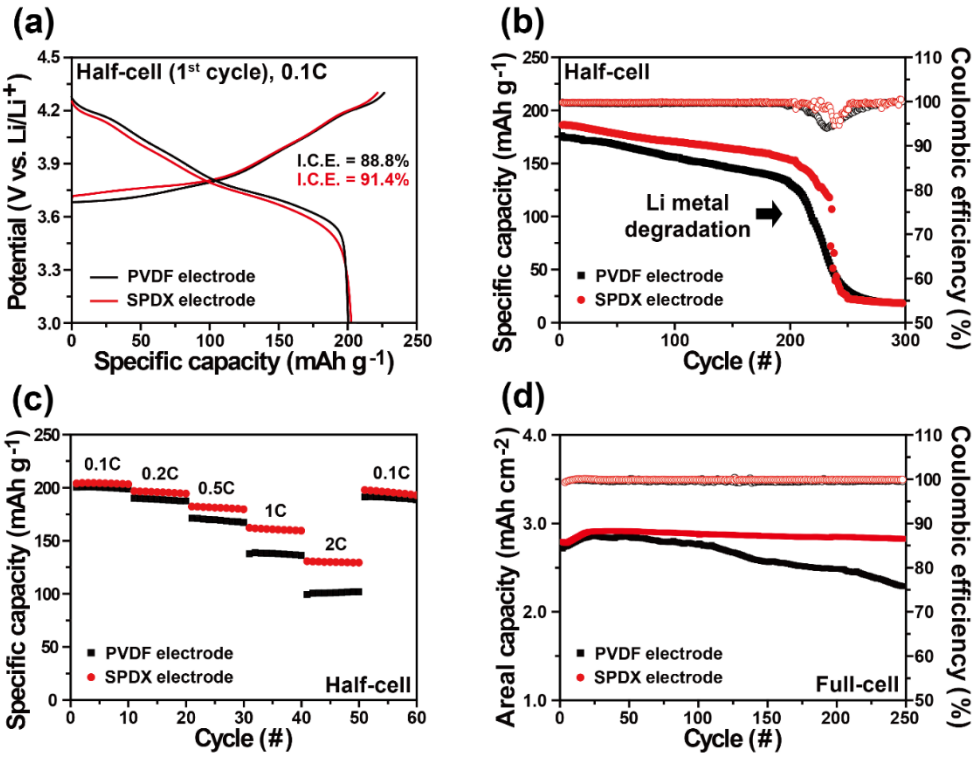

Figure 1.7. Electrochemical performance of the PVDF- and SPDX-based electrodes in (a-c) half-cell and (d) full-cell configurations. (a) Voltage profiles of the PVDF- and SPDX-based electrodes in their first cycle. (b) Capacity retentions and Coulombic efficiencies of both electrodes in the voltage window of 3.0–4.3 V when measured at 0.5C (1C=185 mA g^{-1}). (c) Rate capabilities when measured at various C-rates in the voltage window of 3.0–4.3 V. (d) Capacity retentions and Coulombic efficiencies of the PVDF- and SPDX-based full-cells paired with graphite anodes when measured at 0.5C in the voltage window of 2.8–4.2 V. The loadings of NCM811 were 16.3 mg cm^{-2} for all the results in this Figure.

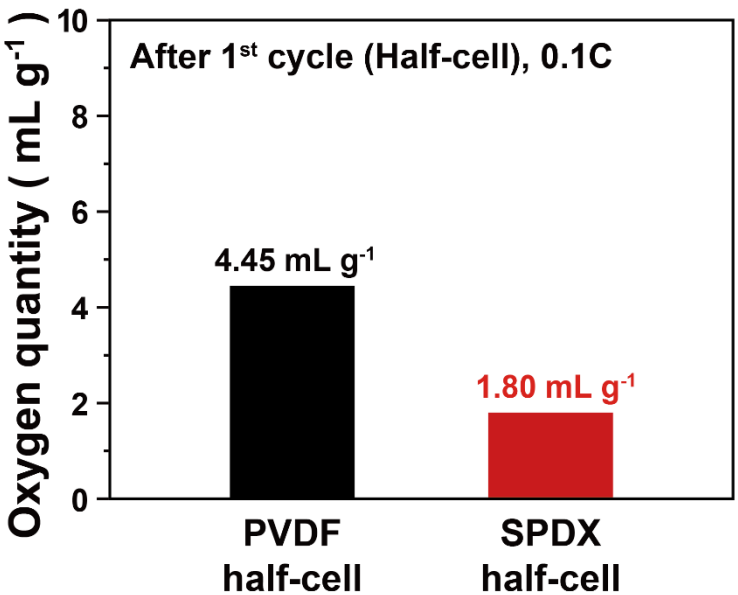

Figure 1.8. Amounts of oxygen generated in the PVDF- and SPDX-based half-cells during the first cycle measured *via* gas evolution analysis.

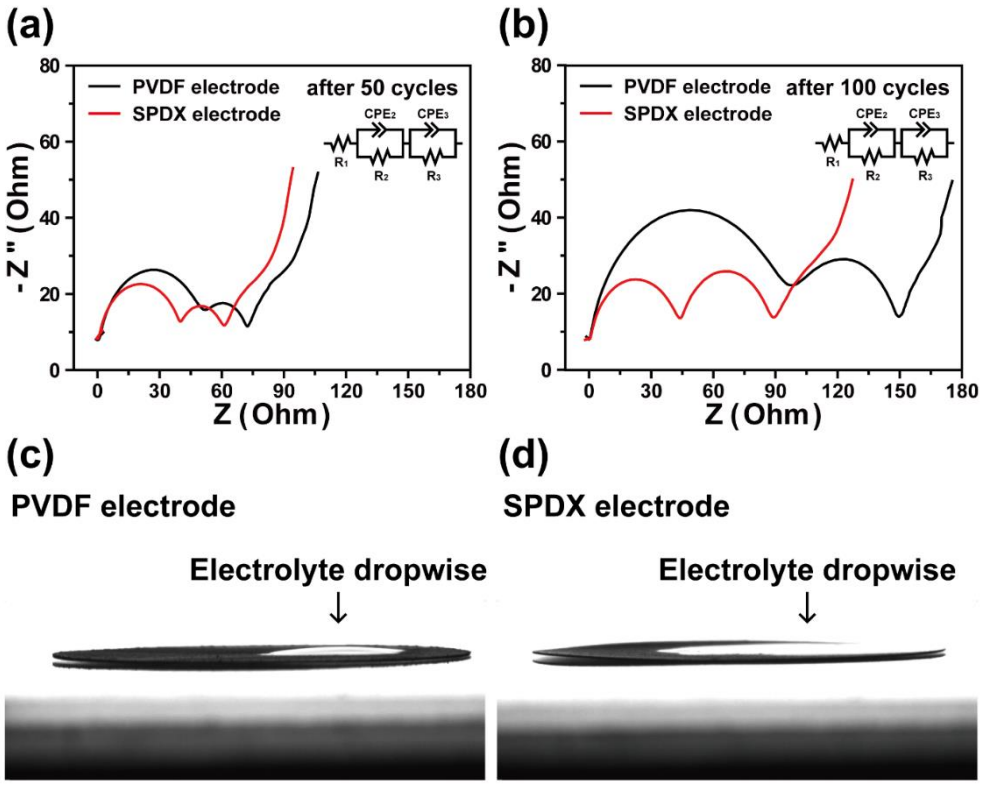

Figure 1.9. Nyquist plots of the PVDF- and SPDX-based electrodes after (a) 50 and (b) 100 cycles. (Inset) The equivalent circuit used to configure each resistance component. Digital photographs after dropping the same amount of organic carbonate-based electrolyte (1 M $LiPF_6$ in EC/DMC (v/v=1:1) + 10 wt % FEC, 5 μL) onto the (c) PVDF- and (d) SPDX-based electrodes.

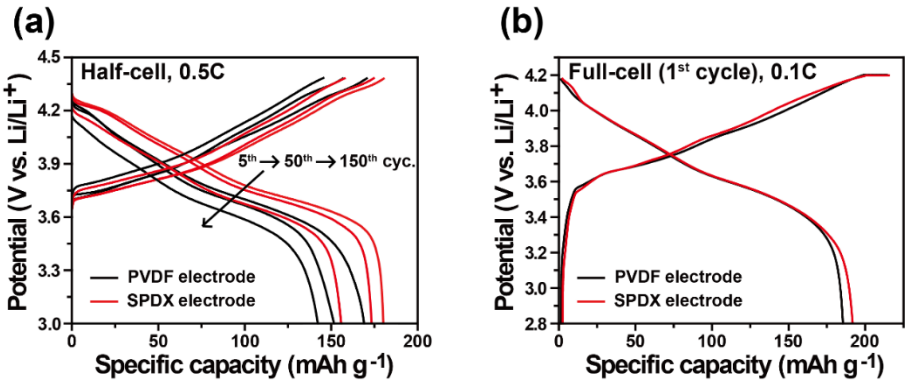

Figure 1.10. (a) Voltage profiles of the PVDF- and SPDX-based half-cells at the 5th, 50th, and 150th cycles. (b) Voltage profiles of the PVDF- and SPDX-based full-cells in their first cycle.

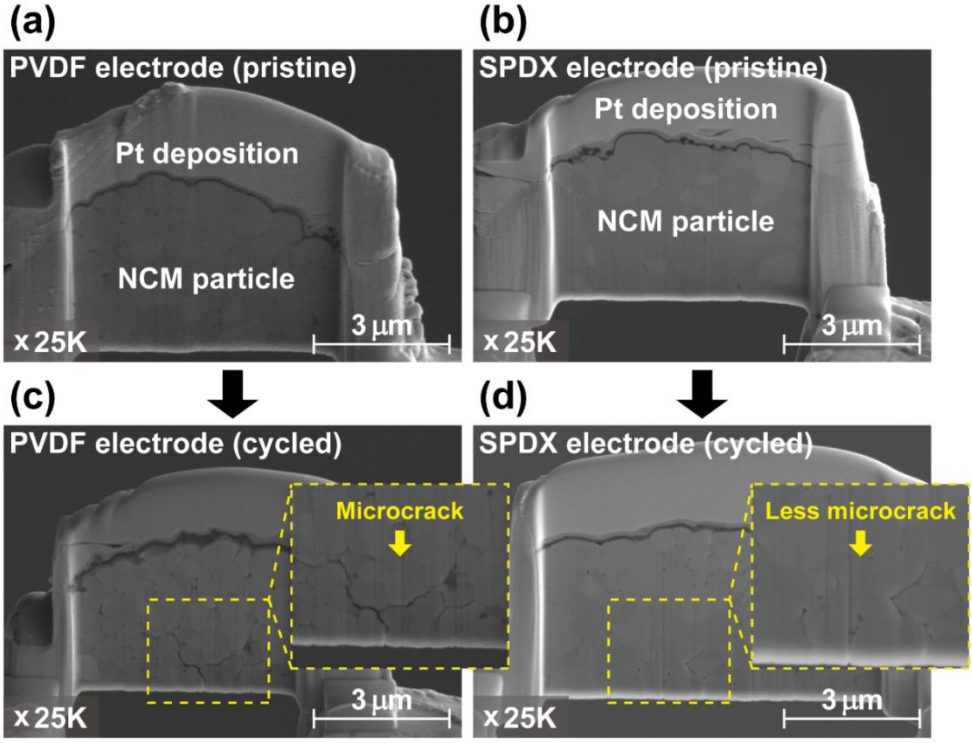

Figure 1.11. Effect of binder selection on micro-crack formation in the NCM particle. FIB-SEM images of the (a) PVDF- and (b) SPDX-based electrodes in the pristine state. FIB-SEM images of the (c) PVDF- and (d) SPDX-based electrodes after 100 cycles.

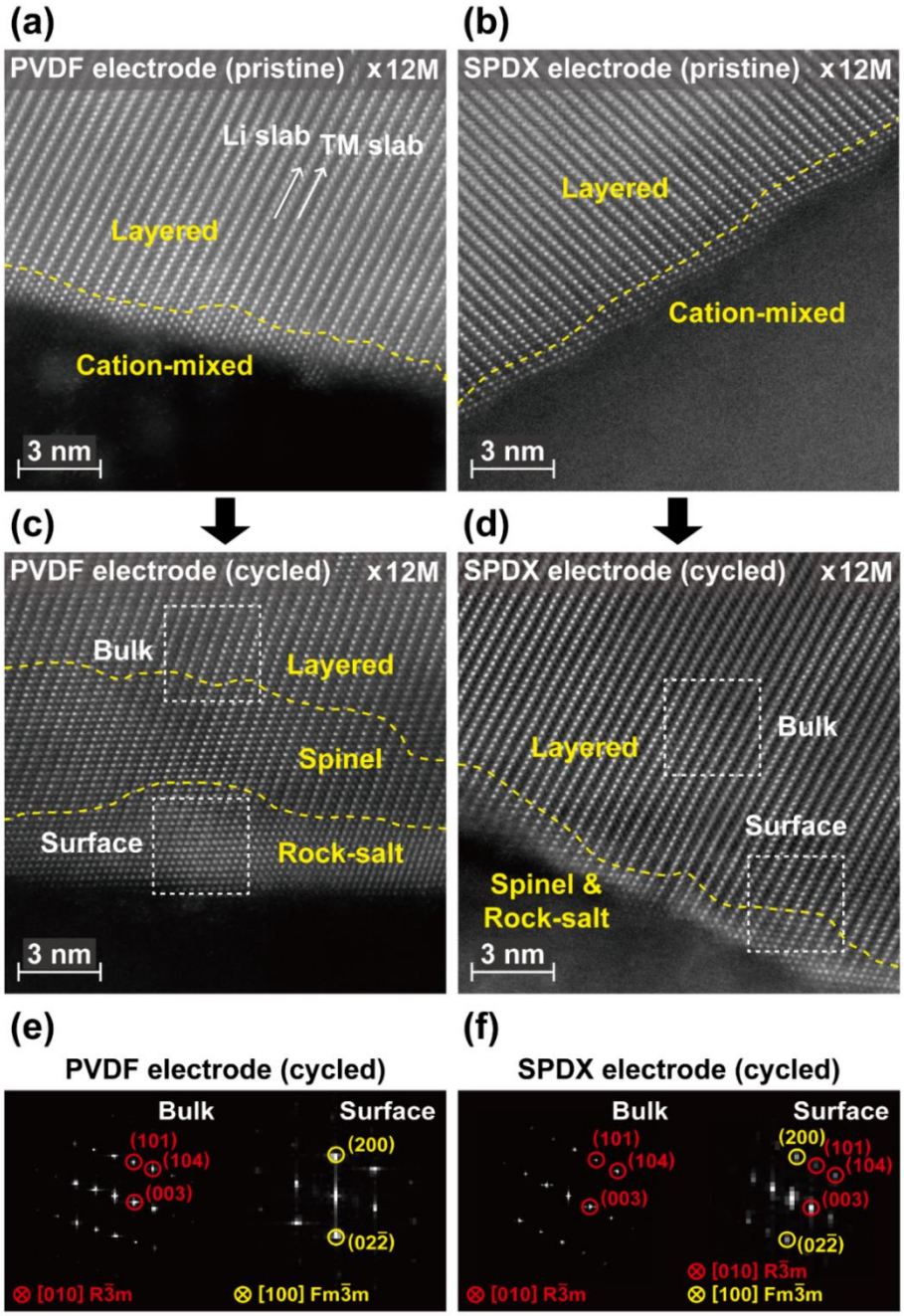

Figure 1.12. Phase transitions near the surface of the NCM particle. HAADF-STEM images of the (a) PVDF- and (b) SPDX-based electrodes in the pristine state. HAADF-STEM images of the (c) PVDF- and (d) SPDX-based electrodes after 100 cycles. (e, f) FFT patterns obtained from the white dotted boxes in (c) and (d), representing the bulk and surface regions of the respective cycled electrodes.

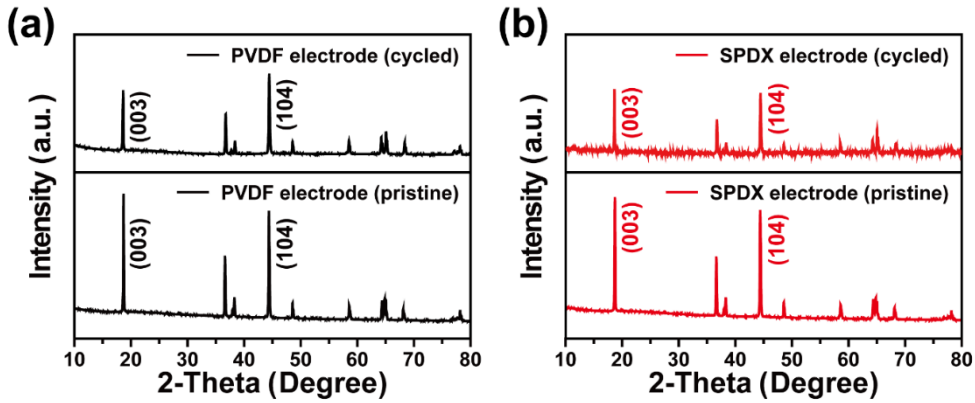

Figure 1.13. XRD analysis before and after cycling. *Ex situ* XRD patterns of the (a) PVDF- and (b) SPDX-based electrodes in the pristine state and after 100 cycles.

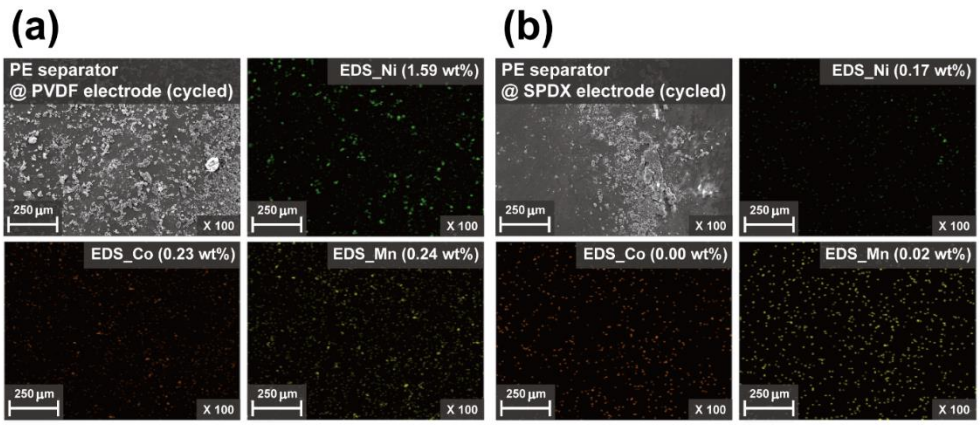

Figure 1.14. Ex situ SEM images of the PE separators of the (a) PVDF- and (b) SPDX-based full-cells after 250 cycles and their corresponding EDS elemental mapping with respect to Ni, Co, Mn. These images and maps were obtained from the graphite anode sides of the PE separators.

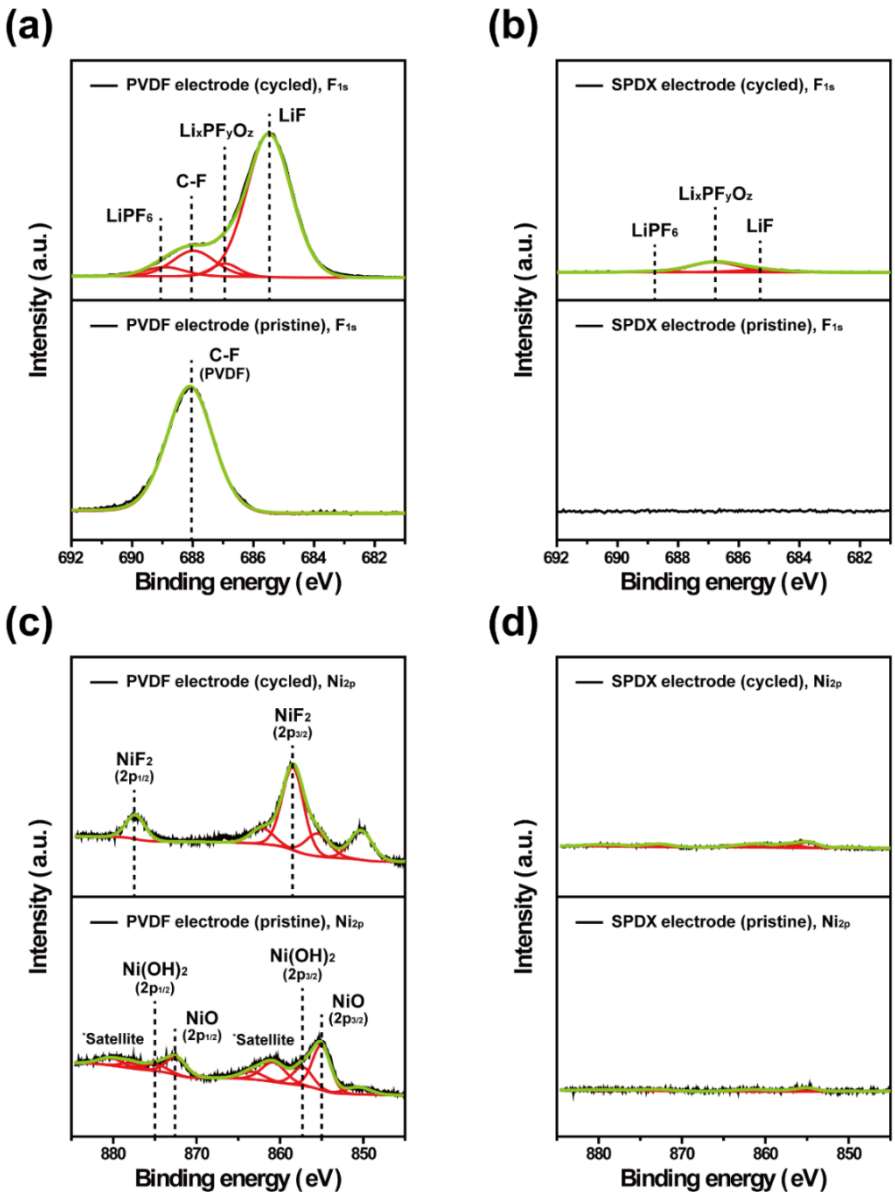

Figure 1.15. Characteristics of F- and Ni-containing bonds in the CEI layer or near the NCM surface. F 1s XPS spectra of the (a) PVDF- and (b) SPDX-based electrodes in the pristine state and after 100 cycles. Ni 2p XPS spectra of the (c) PVDF- and (d) SPDX-based electrodes in the pristine state and after 100 cycles.

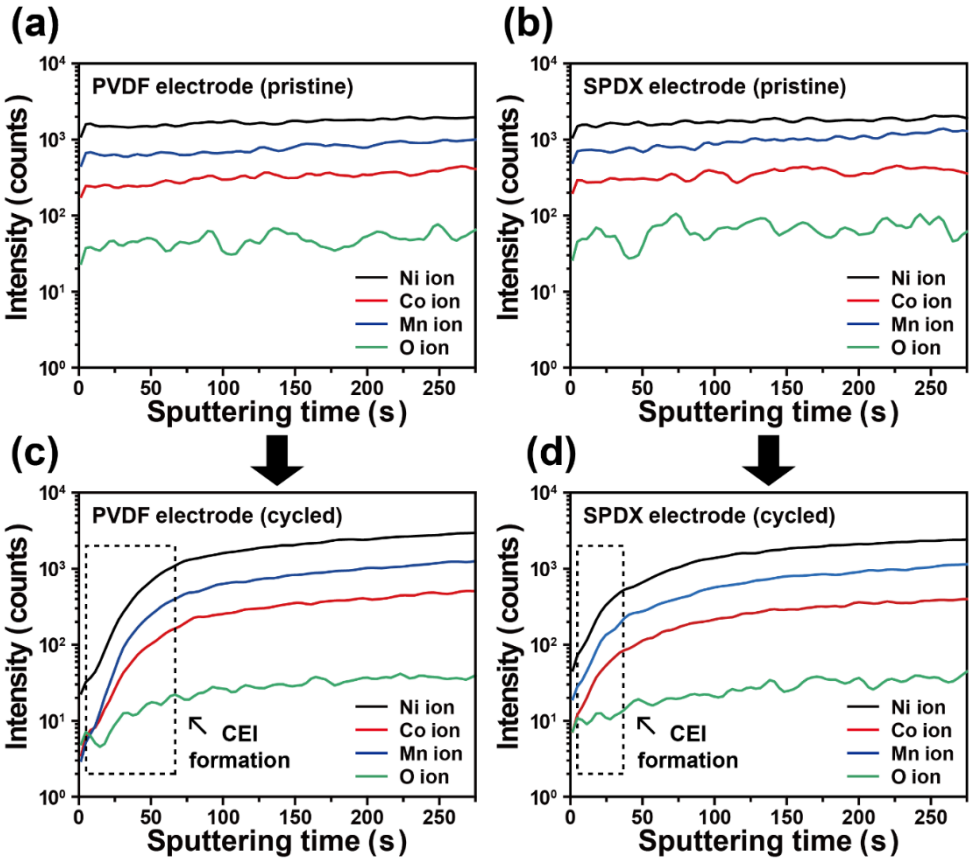

Figure 1.16. ToF-SIMS depth profiles with respect to Ni, Co, Mn, O ions of the (a) PVDF- and (b) SPDX-based electrodes in the pristine state. (c–d) Same analyses after 100 cycles.

Sample	Height parameter			
	S_a[1] (µm)	S_p[2] (µm)	S_v[3] (µm)	S_z[4] (µm)
PVDF electrode (pristine)	3.1	17.2	24.7	41.9
SPDX electrode (pristine)	1.9	12.0	21.0	33.0

[1] Arithmetic mean height; [2] Maximum peak height; [3] Maximum pit height; [4] Maximum height

Table 1.1. CLSM height parameters of the PVDF- and SPDX-based electrodes in the pristine state.

Sample	Concentration of elements (ppb=μg L^{-1})		
	Ni	**Co**	**Mn**
PVDF_24 h	167.5	29.3	220.4
SPDX_24 h	124.6	25.6	210.2
PVDF_36 h	325.7	32.4	286.9
SPDX_36 h	246.6	32.2	261.7
PVDF_2 wk	879.1	192.3	1237.8
SPDX_2 wk	558.9	148.1	559.6

Table 1.2. Concentrations of TM ions dissolved from the PVDF- and SPDX-based electrodes that underwent 250 cycles in a full-cell configuration.

Chapter 2. Sacrificial Binder for 5 V $LiNi_{0.5}Mn_{1.5}O_4$ Spinel Cathodes in Lithium-Ion Batteries

2.1 Introduction

The spinel $LiNi_{0.5}Mn_{1.5}O_4$ (LNMO) offers a high redox potential of 4.7 V vs. Li/Li^+ for lithium (Li) ion storage, which translates into a high energy density of ~650 Wh kg^{-1} at the cell level.[1-3] Additional advantages of LNMO are its low cost, environmental friendliness, and competitive rate performance. Nevertheless, the high operating voltage of LNMO causes it to undergo unwanted reactions with the electrolyte, resulting in degradation of the cathode interface, and leading to deteriorative capacity fading upon cycling.[4] The decomposition of carbonate electrolytes (commonly used in lithium-ion batteries (LIBs)) above 4.4 V vs. Li/Li^+ induces the formation of a thick and unstable cathode-electrolyte interphase (CEI),[5, 6] and the thick CEI layer imposes high interfacial resistance and therefore impairs the cyclability of the given electrode. Thus, the high-voltage operation and limited cycle life of LMNO cathodes have long been considered an inevitable trade-off. Another deleterious degradation mechanism involves lithium hexafluorophosphate ($LiPF_6$), a commercial Li salt widely used in the carbonate electrolytes; at high voltages, $LiPF_6$ can react with traces of water to generate hydrogen fluoride (HF), which triggers the dissolution and migration of transition metal (TM) ions from the surface of the cathode.[7-9] The dissolution of TM ions is accelerated when the bare LNMO surface is exposed to the electrolyte. The dissolved TM ions settle on the anode/cathode surfaces in the form of metallic particles to further catalyze undesired parasitic reactions at both interfaces.[10, 11]

Various strategies have been proposed thus far to suppress the parasitic reactions of the electrolyte, such as the use of electrolyte additives,[12-14] radical

scavengers,[15] and application of protective layers.[8, 16, 17] A variety of inorganic and organic materials[18-20] have been adopted as protective layers to prevent direct contact between the electrolyte and LNMO particles. However, most of these strategies have resulted in limited improvement because the complete coverage of active particles with protective layers is technically infeasible. Even if complete coverage could be accomplished, this could raise the interfacial resistance.[16, 21] Radical scavengers can also perturb the electrolyte conditions or may not be able to eliminate HF molecules completely. On the other hand, binders with the ability to protect the active material while continuing to fulfill their original role of securing inter-particle cohesion and adhesion between the active electrode layer and the current collector have also been pursued.[22, 23] Accordingly, we hypothesized that the binder, in conjunction with the electrolyte, could have a significant impact on the formation and properties of the cathode interface, which are closely linked to the key electrochemical performance metrics of a cell.

Clearly, the aforementioned surface degradation processes become prominent at high operating potentials (i.e., >4.3 V *vs.* Li/Li^+).[6, 7, 24] Although poly(vinylidene fluoride) (PVDF) is the most widely used binder for layered metal oxide cathodes owing to its low interfacial resistance and high oxidative stability,[25, 26] PVDF is unlikely to be beneficial for LNMO cathodes because its non-uniform coverage of the active material, associated with weak van der Waals interaction, may not be able to resolve the aforementioned interfacial issues. As alternatives to PVDF, biopolymers[15, 23, 27] and synthetic polymers[28, 29] have been investigated to take advantage of their hydroxyl or negatively charged functional groups that can participate in hydrogen bonding and ion-dipole interactions, respectively, with the LNMO surface.[30] These strong, well-defined bonding interactions are aligned to uniformly cover the LNMO surface and thus prevent undesired side reactions. However, the uniform coverage of these binders, in turn, increases the interfacial resistance because from a structural viewpoint, they do not usually support Li ion

conductivity.[15, 28, 31, 32]

Having noted that the functionality of a binder has a critical effect on the Li ion diffusion at the CEI layer, we anticipated the possibility of decomposing oxidatively weak functional groups on the binder at high voltages and subsequent transformation of these groups into certain moieties in the CEI layer. With this rationale in mind, the functional groups of a binder can be chosen such that the moieties remaining after decomposition form CEI/binder complexes that are conductive to Li ions to facilitate Li ion diffusion in the CEI. Thus, the binder can behave "sacrificially." Although an electrolyte additive could be designed with a similar purpose, additives could perturb the anode interface[33, 34] because the lowest unoccupied molecular orbital levels of most electrolyte additives are lower than the operating potentials of the anode. Apparently, the main backbone of the binder must retain its adhesive properties by utilizing other functional groups, emphasizing multi-functionality as a key design principle of a binder for LNMO cathodes.

While searching for sacrificial functional groups that could enhance the Li ion conductivity, our attention was attracted to sulfate groups because they were reported to improve the CEI stability when incorporated in electrolyte additives[35, 36] and coating materials.[19, 37] Based on this structural reasoning, we adopted λ-carrageenan (CRN), a bio-inspired seaweed polysaccharide with the sulfate functionality, as a binder for the 5 V LNMO cathodes. CRN has both sulfate and hydroxyl groups on its main backbone (Figure 1a), allowing it to function as a sacrificial and adhesive binder simultaneously, respectively. These two functions were targeted to catch two challenging rabbits at the same time when working with 5 V LNMO: good coverage of the active particles based on strong adhesion and high Li ion conduction at the cathode interface. Moreover, the two functional groups accomplish their individual missions independently, and are therefore orthogonal. To demonstrate the effects of the two functional groups of CRN, sodium alginate (ALG,

Figure 1b) and PVDF (Figure 1c) were chosen as control binders. ALG is structurally highly similar to CRN except that ALG is devoid of sulfate groups. ALG has long been used as an aqueous binder for both cathodes[38-40] and anodes.[41, 42] To the best of our knowledge, the current study is the first case in which the "sacrificial" concept is demonstrated for the binder in LIB cathodes.

2.2 Experimental Section

Preparation of LNMO electrodes. The cathode was fabricated by combining $LiNi_{0.5}Mn_{1.5}O_4$ (LNMO, MTI, USA) powder, Denka black (DENKA, Japan), and the respective binder. Different kinds of binder solutions were used in this experiment. λ-carrageenan (CRN, TCI, Japan) and sodium alginate (ALG, Sigma Aldrich, USA) are water soluble; thus, the binder solutions comprising CRN and ALG were obtained by dispersing a certain amount of each binder in distilled water. In the case of poly(vinylidene fluoride) (PVDF, Mw = 350,000, Kureha, Japan), *N*-methyl-2-pyrrolidone (NMP, SAM CHEON, South Korea) was used as solvent for the binder solution. The working electrode was fabricated by homogeneously mixing the active material, conducting agent, and respective binder in a weight ratio of 90:5:5. The slurry was cast onto the Al current collector using a doctor blade and dried at 100 °C in air for 1 h, and then dried in a vacuum oven at 80 °C overnight. The areal loading of LNMO was 2.0 or 10.0 mg cm^{-2}. CR2032 coin-type cells were prepared to investigate the electrochemical properties of each binder-based electrode. A half-cell consisting of the LNMO cathode and Li foil as the counter electrode was assembled in an Ar-filled glove box, where the oxygen and water contents were below 0.1 ppm, respectively. Polyethylene (PE, W-SCOPE, Japan) and 1 M $LiPF_6$ in ethylene carbonate (EC)/dimethyl carbonate (DMC) (1/1 = v/v) (Enchem, South Korea) were used as separator and electrolyte, respectively.

Characterization. Fourier transform infrared (FT-IR, spectrum 400, Perkin-Elmer, USA) spectra of the CRN, ALG, and PVDF were recorded to identify the functional groups of each binder. Top-viewed images of the pristine and cycled electrodes were acquired by field emission scanning electron microscopy (FE-SEM, JSM-7500F, JEOL, Japan and Verios 5 UC, Thermo Fisher Scientific, USA). The surface morphology and binder coverage on active materials were analyzed using Cs-corrected transmission electron microscopy (TEM, JEM-ARM200F, JEOL, Japan) at an acceleration voltage of 80 kV. The chemical bonds of the CEI/binder complex of each electrode were characterized using X-ray photoelectron spectroscopy (XPS, K-ALPHA+, Thermo Fisher scientific, USA). The mass spectra of the CEI/binder complex components of each electrode were characterized *via* time-of-flight secondary ion mass spectroscopy (ToF-SIMS, TOF-SIMS 5, ION-TOF GmbH, Münster, Germany) in the KBSI Busan Center using a pulsed 30 keV Bi_3^+ primary beam with a current of 0.60 pA. ToF-SIMS depth profiles were acquired from a sputtered square area of 500 μm × 500 μm using an Ar-cluster of 10 keV. Reconstructed ToF-SIMS spectra were extracted from the ToF-SIMS depth profile by selecting a specific sputtering time (0 and 40 sec). The electrical resistance of each electrode was measured by a four-point probe system (CMT-100S, AIT, South Korea). Solid-state ^{7}Li nuclear magnetic resonance (^{7}Li-NMR, 500 MHz Avance III HD, Bruker, Germany) spectra were recorded to compare the electron densities of $LiSO_3F$ (Synquest Laboratory, 95%, USA) and LiF (Sigma-Aldrich, 99.99%, USA) near the Li atom using 4 mm CP-MAS probes. The spinning speed of 10 kHz and pulse repetition delays of 5 s were used.

Electrochemical measurement. Galvanostatic charge/discharge tests were conducted on a battery cycler (WBCS 300L, WonATech, South Korea) in the voltage range of 3.5–5.0 V (*vs.* Li/Li^+) for the LNMO/Li half-cells. Prior to the electrochemical tests, all cells were rested for 5 h to enable the electrodes to become

sufficiently soaked with electrolyte. The cycle life and Coulombic efficiency (CE) of the LNMO/Li half-cells were measured at room temperature and 45 °C at 1C after three formation cycles which were scanned at 0.1C to stabilize the CEI. The rate capability was investigated by scanning at various C-rates from 0.1C to 5C. The electrochemical floating test, conducted in the LNMO/Li half-cells, was monitored by a potentiostat (VMP3, Bio-logic, France). The cells were charged to 4.6 V at a rate of 0.1C, whereupon the voltage was increased to 5.0 V step by step in increments of 0.1 V and each voltage level was maintained for 10 h. After raising the voltage to 5.0 V, the LNMO/Li half-cells were discharged to 3.5 V at a rate of 0.1C and the procedure above was repeated twice. The electrochemical stability of the binder-conducting agent composite films (1:1, w/w) was evaluated by cyclic voltammetry (CV) in the 3.5–5.0 V voltage window at a scanning rate of 0.05 mV s^{-1} and CV measurements of the LNMO/Li half-cells were carried out on the potentiostat at various scanning rates. Electrochemical impedance spectroscopy (EIS) analysis of the LNMO/Li half-cells was performed using the potentiostat over the frequency range of 0.01 Hz–1 MHz and at the amplitude of 10 mV.

DFT calculation. Geometric optimization and single-point energy calculation to gain the binding energy of Li ion in the molecule were conducted based on the three-parameter Becke model with the Lee-Yang-Par modification (B3LYP) in the GAUSSIAN16 software package. The basis set that was used in this study is 6-311++G (3df,3pd) containing diffusive functions to accommodate the charge in molecular systems. The binding energy of Li ion in the molecule was calculated starting with optimization of the geometry of a molecule followed by single-point energy calculation. The optimized molecular structure was then divided into a single-anion model and Li ion model for the geometrical optimization and single-point energy calculation. The single-point energies for the molecule, the single anion, and Li ion were then used to calculate the binding energy.

2.3 Results and Discussion

The binder coverage on the LNMO surface in the pristine state was investigated using transmission electron microscopy (TEM). In the case of the polysaccharide-based electrodes, the coverage of the CRN and ALG binders was thin and uniform along the LNMO surface (Figure 1d and e, respectively), which is attributed to their hydrophilic functional groups. The Fourier-transform infrared (FT-IR) spectra (Figure 2) of these two binders verified the presence of the hydroxyl and carboxyl groups; the O–H stretch mode in the hydroxyl group, and the C=O and C–O stretch modes in the carboxylic group were detected at ~3400, ~1700, and ~1100 cm^{-1}, respectively. These functional groups form hydrogen bonding or ion-dipole interactions with the oxygen in the TM–O bonds on the LNMO surface. In contrast, in the case of the PVDF-based electrode, the PVDF was not evenly distributed as it was locally agglomerated on the LNMO surface (Figure 1f). This can be explained by the fact that the weak van der Waals interaction of PVDF, as suggested by its FT-IR spectrum (Figure 2), did not induce tangible adhesion with the active material. Furthermore, polysaccharides can function as surfactants[43, 44] to ensure that the other electrode components are well dispersed in the aqueous slurry as well as in the electrode. The top-view scanning electron microscopy (SEM) images (Figure 3a and b) consistently showed that the conducting agent was more homogeneously dispersed in the CRN- and ALG-based electrodes than in the PVDF-based electrode (Figure 3c). The more optimal dispersion of the conductive agent in the CRN- and ALG-based electrodes was reflected in the higher electronic conductivities of these two electrodes compared to that of their PVDF-based counterpart, based on the 4-point analysis (Figure 3d).

To prove that the sulfate functional groups in the CRN are indeed electrochemically decomposed, electrochemical floating tests were performed in the three-electrode configuration during the first and third formation cycles (Figures 1g–

j). In these floating tests, constant potential was applied for 10 hours at each voltage level while the specific current was monitored. The charging process in the first formation cycle was characterized by continuous peak-less curves for both the ALG- and PVDF-based electrodes (Figure 1g). However, for the CRN-based electrode a shoulder peak was observed at 4.8 V (arrow in Figure 1g), which is more clearly visible in the magnified view in Figure 1h. The presence of this shoulder peak on the curve of only the CRN-based electrode is attributed to the oxidative decomposition of its sulfate functional groups, rather than to the leakage current related to electrolyte decomposition. The shapes of the current profiles of all the electrodes became similar in the third formation cycle (Figure 1i and j), which indicates that the oxidation of the CRN in the initial charging process was irreversible, and that the electrode stabilized thereafter. This result is in line with those in reports about electrolyte additives;[45-47] lithium sulfate derivatives derived from the CRN are formed on the LNMO surface during the initial charging process and are not further oxidized once an electronically insulating interfacial layer is established in the early cycles. The cyclic voltammetry (CV) tests of the respective binders were consistent with these results and exhibited a similar trend (Figure 4).

The electrochemical performance of the electrodes based on the three binders was evaluated by conducting galvanostatic measurements after fabricating coin-type half-cells. For these tests, the cells first underwent three formation cycles in the voltage range of 3.5–5.0 V (*vs.* Li/Li^+) at 0.1C (14.7 mA g^{-1}) (Figure 5). The initial Coulombic efficiencies (ICEs) of the CRN-, ALG-, and PVDF-based cells in the first formation cycles were 90.3%, 91.5%, and 88.8%, respectively (Figure 5a). The higher ICEs of the CRN- and ALG-based cells are attributed to their more uniform surface coverage that protects the LNMO from the electrolyte. Between the CRN- and ALG-based cells, the lower ICE of the CRN-based one resulted from its irreversible oxidative decomposition at high voltages, which agrees well with the aforementioned electrochemical floating test results (Figure 1g and h). Owing to the

uniform coverage of the CRN and ALG binders, the overpotentials of these two cells during the first formation cycles were slightly higher. However, the overpotentials of the CRN- and ALG-based cells gradually decreased within the first three formation cycles because of the stabilization of the CEI layers, whereas that of the PVDF-based cell increased (Figure 5b). These distinct overpotential behaviors of the cells were reflected in the higher discharge capacity of the CRN-based cell (131.0 mAh g^{-1}) in the third formation cycle compared to those of its ALG-based (127.3 mAh g^{-1}) and PVDF-based (127.1 mAh g^{-1}) counterparts. These series of results inform that the stability of the CEI/binder complex is greatly determined in the first formation cycles, and that the binder plays a crucial role in the stability of this complex.

Figure 6a shows the cycling performance of the three cells at 1C (1C = 147 mA g^{-1}) and room temperature in the potential range of 3.5–5.0 V vs. Li/Li^{+} after three formation cycles. The CRN-based cell displayed superior performance compared to those of its PVDF- and ALG-based counterparts in terms of both the cyclability and specific capacity. The CRN-, ALG-, and PVDF-based cells delivered first reversible capacities of 110.7, 96.1, and 112.0 mAh g^{-1}, respectively, and retained 100.0%, 98.6%, and 75.4% of their original capacities after 900 cycles. The average CEs of the three cells were 99.6%, 99.6%, and 99.4%, respectively. These distinct performances can be explained by the properties of the binders: the uniform coverage by the polysaccharide binders of the LNMO surface mitigate surface degradation to more effectively sustain cycling. Between the two polysaccharide binders, the ion conductive characteristics of the CEI induced by the decomposition of the sulfate groups endows the corresponding cell with higher specific capacity. The distinct capacities between the two polysaccharide binders remained unchanged; the specific capacities of the CRN- and ALG-based cells at the 900th cycle were 110.7 and 94.7 mAh g^{-1}, respectively. Even at a higher mass loading (10 mg cm^{-2}) of the active material, the CRN-based cell outperformed its PVDF- and ALG-based

counterparts in terms of both the cyclability and specific capacity (Figure 7), which highlights once again the role of the Li-ion conductivity of the CEI/binder complex in the CRN-based electrode. In addition, the trends of the cycling stability and specific capacity were preserved even at 45 °C (Figure 8).

The SEM images (Figure 9) of the electrodes after 100 cycles reveal that the adhesion strengths of the respective binders are clearly different. The polysaccharide-based electrodes exhibited denser particle packing (Figure 9a and b), even after 100 cycles, compared to the PVDF-based electrode (Figure 9c). This tendency is more conspicuous in the enlarged images (Figures 9d–f). The stronger adhesion of the polysaccharide-based electrodes is also revealed in their digital photographs (Figure 10). The CRN- and ALG-based electrodes remained firmly attached to the Al current collectors after 100 cycles unlike the PVDF-based one, which largely peeled off after the same number of cycles. These results imply that the CRN-based electrode retained its adhesive properties during cycling involving oxidative decomposition.

The binder also markedly affects the rate performance. When swept between 0.1C and 5C, the discharge capacity of the CRN-based cell remained far higher (Figure 6b), clearly taking advantage of the Li-ion conductivity of its CEI/binder complex. For example, at 5C, the specific capacities of the CRN-, ALG-, and PVDF-based cells were 81.3, 59.7, and 36.3 mAh g^{-1}, respectively. The distinct rate performance among the three cells was elucidated by electrochemical impedance spectroscopy (EIS) analysis for the pristine and 100-cycled states (Figure 6c and d). The Nyquist plots of all the electrodes were fitted using an equivalent circuit model (Figure 11). The CEI resistance (R_{CEI}) and charge-transfer resistance (R_{CT}) are closely related to the interfacial resistance of the LNMO surface. In the pristine state (Figure 6c), the polysaccharide-based cells exhibited higher interfacial resistances (305.0 and 343.1 Ω for the CRN- and ALG-based cells, respectively) than the PVDF-based electrode (139.5 Ω) because of the more uniform coverage of the

polysaccharide binders. After 100 cycles (Figure 6d), both the R_{CEI} and R_{CT} of the CRN-based cells (4.5 and 88.9 Ω, respectively) were lower than those of the ALG-based (7.2 and 155.1 Ω, respectively) and PVDF-based (64.2 and 252.9 Ω, respectively) cells. This result again reflects the benefit of the Li-ion conductivity of the CEI/binder complex formed by the sacrificial function of the sulfate groups in the CRN. Both the R_{CEI} and R_{CT} of the PVDF-based electrode significantly increased over the cycling period of 100 cycles, which reflects the destabilization of the interface because of the limited coverage provided by PVDF. Detailed interfacial resistance values are provided in Table 1. In addition, CV at various scan rates from 0.05 to 1 mV s^{-1} was used to investigate Li ion transport through the LNMO surface (Figure 12). The lithium-ion diffusion coefficient (D_{Li+}) can be extracted from the relationship between i_p and $v^{1/2}$ as expressed by the following equation:[48, 49]

$$i_p = 2.69\times10^5\times n^{3/2}\times A\times D_{Li+}{}^{1/2}\times v^{1/2}\times C_{Li+}, \quad (1)$$

where i_p is the peak current, n is the number of electrons per reaction species (n = 1 for the LNMO cathode), A is the surface area of the electrode, v is the scan rate, and C_{Li+} is the bulk concentration of Li ions in the electrode (0.02378 mol cm^{-3}).[50, 51] Using the slopes of the i_p *vs.* $v^{1/2}$ plots, the D_{Li+} values of the CRN-, ALG-, and PVDF-based electrodes were calculated to be 2.84×10^{-10}, 1.81×10^{-10}, 8.98×10^{-11} cm^2 s^{-1}, respectively (Figure 6e). These results are consistent with the tendencies exhibited by the rate performance and EIS results and are ascribed to the efficient Li ion migration through the Li-ion-conductive CEI/binder complexes of the CRN-based electrode.

The characteristics of the CEI/binder complex in the CRN-based electrode were examined by subjecting all three electrodes to X-ray photoelectron spectroscopy (XPS) analysis (Figures 13a–d). The O 1s spectra of the pristine CRN-, ALG-, and PVDF-based electrodes displayed signals corresponding to the TM–O bond in the LNMO particles (Figure 14). The intensity of the TM–O peak of the

PVDF-based electrode at 529.88 eV was higher than those of the CRN- and ALG-based electrodes, pointing to the greater extent of exposure of the exterior surface of LMNO owing to the non-uniform coverage afforded by PVDF. This observation is consistent with the TEM results of the pristine electrodes (Figures 1d–f), according to which the polysaccharide binders offer more uniform coverage of the LNMO surface.

Figures 13a–c displays the F 1s XPS profiles of the CRN-, ALG-, and PVDF-based electrodes, respectively, at three different cycling stages: pristine, after 3 cycles, and after 100 cycles. In the pristine state, no signal was observed for the CRN- and ALG-based electrodes; however, a peak ascribed to the strong C–F bond of the PVDF in the PVDF-based electrode was observed. After 3 cycles, peaks related to LiF and $Li_xPO_yF_z$ were observed for the CRN- and ALG-based electrodes (Figure 13a and b), originating from the decomposition of the PF_6^- anion. The CRN-based electrode additionally exhibited a peak at 687.98 eV, assigned to $LiSO_xF$. The identification of this peak was confirmed by comparison with commercial $LiSO_3F$ (Figure 15a). In contrast, the peaks of these inorganic species did not feature prominently on the spectra of the PVDF-based electrode (Figure 13c). After 100 cycles, the LiF in the CRN- and ALG-based electrodes decreased whereas the $Li_xPO_yF_z$ increased (Figure 13a and b). The $LiSO_xF$ in the CRN-based electrode also decreased. By contrast, the PVDF-based electrode exhibited a far greater increase in both LiF and $Li_xPO_yF_z$ during the same cycling period (Figure 13c). Considering that the probing depth of XPS is around 5 nm,[52] we anticipate that the LiF (also, $LiSO_xF$ for the CRN-based electrode) that had formed during the early cycling period in the CRN- and ALG-based electrodes was gradually covered by other CEI components such as $Li_xPO_yF_z$., as cycling progressed. Contrary to this, the portions of both LiF and $Li_xPO_yF_z$ increased with cycling in the case of the PVDF-based electrode. The evolution of the surface components led us to elaborate the reactions as follows:

$$LiPF_6 \rightarrow LiF + PF_5 \quad (2)$$

$$LiPF_6 + H_2O \rightarrow 2HF + POF_3 + LiF \quad (3)$$

$$PF_5 + H_2O \rightarrow POF_3 + 2HF \quad (4)$$

In reaction (2), the anionic functional groups from the CRN and ALG binders (sulfate and carboxylate, respectively) can largely stabilize the Lewis acidic PF_5. Therefore, during the early cycling period, these functional groups could drive reaction (2) forward particularly in the vicinity of the LNMO surface where the polysaccharide binder was accessible, leading to the formation of LiF on the surface of LNMO. Previous studies[53-55] reported the anion-induced formation of LiF on the surfaces of cathodes in contact with an electrolyte that contains FSI^- and $TFSI^-$ anions. The formation of LiF on the LNMO surface could therefore play a positive role toward preventing the decomposition of the electrolyte by taking advantage of the insulating nature of LiF. As described above, the PF_5 that formed reacts with traces of water to yield POF_3 (reaction (4)), which ultimately produces $Li_xPO_yF_z$ in the CEI layer. However, in the PVDF-based electrode, reaction (2) would not proceed as readily because PVDF may not be able to stabilize PF_5 as much (Figure 13c). Instead, the PVDF-based electrode undergoes reaction (3) predominantly in the presence of traces of water, producing LiF and POF_3 concurrently throughout cycling. Thus, in the CEI layer, the distribution of LiF in the CEI matrix differs: the LiF in the CEI layer of the polysaccharide-based electrodes occupies the inner CEI layer and is covered by $Li_xPO_yF_z$ in the outer CEI layer, whereas the LiF in the CEI layer of the PVDF-based electrode exists together with $Li_xPO_yF_z$ without forming discrete layers. Therefore, the LiF in the polysaccharide-based electrodes is more compact and therefore more capable of precluding electrolyte decomposition. This compact LiF is often referred to as "good" LiF in contrast to the sparsely distributed "bad" LiF.[2, 56, 57] All in all, careful selection of the CRN binder can lead to a more robust CEI toward warranting more reliable and stable operation of the cell.

The characteristics of the CEI of the CRN-based electrode were further captured in its S 2p XPS results. Doublet peaks associated with the O−SO_3 bond (171.17 and 169.97 eV) were observed for the pristine state (Figure 13d), reflecting the sulfate groups in the bare CRN. In sharp contrast, peaks related to $LiSO_3F$ (170.40 and 169.14 eV) and $LiSO_2F$ (169.58 and 168.38 eV),[58] whose peak positions were confirmed by comparison with commercial $LiSO_3F$ (Figure 15b), became evident after 3 and 100 cycles. After 3 cycles, the peaks at 532.48 eV, assigned to $LiSO_xF$ (x = 2, 3) (Figure 15c), were also detected only in the O 1s branch of the CRN-based electrode (Figure 14a). We attributed the formation of the $LiSO_xF$ (x = 2, 3) to the radical reaction of the sulfate moieties in the CRN with the Lewis acidic PF_5 at high voltages (Figure 16) upon the progression of reaction (2). After 100 cycles, the intensity of the $LiSO_xF$ peaks on the S 2p and O 1s XPS profiles decreased, similar to those of the LiF peaks in the polysaccharide-based electrodes, demonstrating that these components are formed directly above the LNMO surface during complex formation but are barely formed during later cycles. In addition, the sulfate (O−SO_3) peak in the CRN-based electrode was still detected even after 3 and 100 cycles, implying that not all sulfates in the CRN were consumed for the formation of $LiSO_xF$. The presence of $LiSO_xF$ was also detected by time-of-flight secondary ion mass spectrometry (ToF-SIMS) (Figure 13e). Analysis of the mass spectrum of the ejected secondary ion fragments revealed the presence of the anionic fragment of $LiSO_2F^-$ (m/z = 89.98) in the negative mode after 3 cycles as a signature of $LiSO_xF$. The electrochemical floating test results, the O 1s, F 1s, and S 2p XPS results, and the ToF-SIMS mass spectra coherently support our view that the CEI layer in the CRN-based electrode contains $LiSO_xF$ originating from the decomposition of the sulfate functional groups of CRN at high voltage.

On the other hand, the ToF-SIMS mass spectra pertaining to the other components (Figure 17) contain useful information on the CEI/binder complexes. The anionic fragment CH_3O^- (m/z = 31.02)[59, 60] appeared more prominent for the

PVDF-based electrode after 3 cycles compared to its CRN- and ALG-based counterparts (Figure 17). A large number of organic components, stemming from the decomposition of the electrolyte, were more evident for the PVDF-based electrode in reflection of the more vulnerable nature of the organic electrolyte solvents at the cathode interface.

The prevalence of other anionic fragments $LiSO_2F^-$, LiF^- (m/z = 26.00), and $PO_2F_2^-$ (m/z = 100.97) was traced as a function of the sputtering time (Figure 18a). Consistent with the S 2p XPS results, the intensity of the $LiSO_2F^-$ anionic fragment started increasing when sputtering commenced, and the gradual decline in the prominence of this fragment after 40 sec indicated its more concentrated presence in the interior of the CEI. On closer inspection, in the CRN-based electrode, the intensity of the $LiSO_2F^-$ anionic fragment turned out to be higher after 40 sec sputtering compared to before sputtering (Figure 18b). This was distinct from the ALG- and PVDF-based electrodes (Figure 18c and d), which exhibited almost no difference in the peak intensity at the same sputtering times. The depth profiles of the LiF^- anionic fragment, related to the LiF component of the CEI/binder complex, revealed similar anomalies. Unlike the CRN- and ALG-based electrodes, for which the intensity increased during the initial 40 sec and then gradually decreased, as in the case of $LiSO_2F^-$, the intensity of LiF^- in the PVDF-based electrode decreased monotonically from the beginning. These trends were clearly evident from the intensity profiles of the LiF^- ion fragment at 0 and 40 sec sputtering for the three electrodes (Figures 18e–g). Once again, the peak intensity of this ionic fragment is linked to the presence of concentrated LiF in the interior of the CEI/binder complex as induced by the stabilization of the PF_5 Lewis acid in reaction (2) in the formation cycle. By contrast, the intensity of the $PO_2F_2^-$ anionic fragment, related to the $Li_xPO_yF_z$ components of the CEI/binder complex, decreased monotonically throughout the sputtering period for all of the three electrodes (Figure 18a), implicating that $Li_xPO_yF_z$ components were continuously being deposited on the

LNMO particle surface during cycling. The ToF-SIMS depth profile data portray a consistent picture regarding the CEI layer of the CRN-based electrode. That is, the CEI layer is characterized by the formation of $LiSO_xF$ with beneficial LiF in the interior of the layer, which plays an important role in protecting the electrode from unwanted side reactions. The compositions and structures of the CEI layers of the three electrodes based on the analytic results obtained thus far are schematically summarized in Figure 19.

Interestingly, the combined composition of LiSO*x*F/LiF in the interior of the CEI layer of the CRN-based electrode is more beneficial than the exclusive composition of LiF in the interior of the CEI layer of the ALG-based electrode in terms of Li ion diffusion, which can be reconciled with the superior electrochemical rate performance of the CRN-based electrode. These comparative results led us to consider the electrostatics between the Li ion and the counter anions SO_xF^- and F^- of $LiSO_xF$ and LiF, respectively, because the electrostatic force is well known[61-63] to affect the Li ion mobility in the CEI layer. To this end, the binding energies of the Li ion with the counter anions were evaluated via density functional theory (DFT) calculations (Figure 20a). These calculations indicate that the lithium sulfate derivatives ($LiSO_2F$ and $LiSO_3F$) from the CRN have binding energies of −6.27 and −6.67 eV, respectively, which are lower than that of LiF (−8.11 eV), implying that the Li ion interacts less strongly with the anions of $LiSO_xF$ than with that of LiF. In addition, commercial $LiSO_3F$ and LiF were analyzed using solid-state ^{7}Li nuclear magnetic resonance spectroscopy (^{7}Li-NMR) to experimentally verify the results of the above calculation (Figure 20b). Unfortunately, $LiSO_2F$ was not commercially available. According to the ^{7}Li-NMR analysis, the chemical shift of $LiSO_3F$ was lower (−1.44 ppm) than that of LiF (−0.85 ppm), indicating that the higher electron density near the Li atom in the $LiSO_3F$ further shields the nucleus of the Li atom from the external field. This result correlates with the above DFT calculations in that the anion of $LiSO_3F$ engages in weaker binding with the Li ion such that the Li ions

can diffuse more freely.

2.4 Conclusion

Despite representing an advantage, the possibility of the high-voltage operation, 4.7 V vs. Li/Li^+, in turn, constitutes a severe shortcoming of the LNMO cathode as it triggers deteriorative degradation of the electrolyte on the cathode surface. Attempts to stabilize the cathode interface have entailed the use of several strongly adhesive binders to protect the LNMO surface, but this came at the expense of the rate performance because of the resistive nature of the binder. In this work, we overcame this longstanding challenge by employing a sulfated polysaccharide binder, namely, CRN. This binder forms CEI/binder complexes that are highly conductive to Li ions through the irreversible, oxidative decomposition of the sulfate pendant groups under high-voltage conditions. The hydrophilicity of CRN makes it feasible to cover the LNMO particles uniformly, yet the oxidative decomposition of the sulfate groups leads to the formation of the CEI/binder complex layer containing $LiSO_xF$, which facilitates Li ion conduction, enabling us to simultaneously catch two challenging rabbits pertaining to the battery operation of LNMO: high rate and long-term cycling. This study is the first demonstration of the "electrochemically sacrificial" concept in binder design to manipulate the CEI layer. Based on the same principle, a variety of functional groups could be taken into consideration to target emerging LIB electrodes that have superior electrochemical properties but are unfavorably affected by interfacial instability.

2.5 Reference

[1] G. Liang, V. K. Peterson, K. W. See, Z. Guo and W. K. Pang, *J. Mater. Chem. A*, 2020, **8**, 15373-15398.

[2] N.-S. Choi, J.-G. Han, S.-Y. Ha, I. Park and C.-K. Back, *RSC Adv.*, 2015, **5**, 2732-2748.

[3] W. Li, Y.-G. Cho, W. Yao, Y. Li, A. Cronk, R. Shimizu, M. A. Schroeder, Y. Fu, F. Zou, V. Battaglia, A. Manthiram, M. Zhang and Y. S. Meng, *J. Power Sources*, 2020, **473**, 1-9.

[4] A. Manthiram, K. Chemelewski and E.-S. Lee, *Energy Environ. Sci.*, 2014, **7**, 1339-1350.

[5] R. Jung, M. Metzger, F. Maglia, C. Stinner and H. A. Gasteiger, *J. Phys. Chem. Lett.*, 2017, **8**, 4820-4825.

[6] L. Yang, B. Ravdel and B. L. Lucht, *Electrochem. Solid-state Lett.*, 2010, **13**, A95-A97.

[7] J. Ma, P. Hu, G. Cui and L. Chen, *Chem. Mater.*, 2016, **28**, 3578-3606.

[8] K. Liu, Q. Zhang, S. Dai, W. Li, X. Liu, F. Ding and J. Zhang, *ACS Appl. Mater. Interfaces*, 2018, **10**, 34153-34162.

[9] C. Zhan, T. Wu, J. Lu and K. Amine, *Energy Environ. Sci.*, 2018, **11**, 243-257.

[10] M. Matsui, K. Dokko and K. Kanamura, *J. Electrochem. Soc.*, 2010, **157**, A121-A129.

[11] R. Jung, M. Metzger, F. Maglia, C. Stinner and H. A. Gasteiger, *J. Electrochem. Soc.*, 2017, **164**, A1361-A1377.

[12] J. G. Han, K. Kim, Y. Lee and N. S. Choi, *Adv. Mater.*, 2019, **31**, 1804822.

[13] M. Xu, N. Tsiouvaras, A. Garsuch, H. A. Gasteiger and B. L. Lucht, *J. Phys. Chem. C*, 2014, **118**, 7363-7368.

[14] T. Yang, H. Zeng, W. Wang, X. Zhao, W. Fan, C. Wang, X. Zuo, R. Zeng

and J. Nan, *J. Mater. Chem. A*, 2019, **7**, 8292-8301.

[15] Y. Ma, K. Chen, J. Ma, G. Xu, S. Dong, B. Chen, J. Li, Z. Chen, X. Zhou and G. Cui, *Energy Environ. Sci.*, 2019, **12**, 273-280.

[16] J. W. Kim, D. H. Kim, D. Y. Oh, H. Lee, J. H. Kim, J. H. Lee and Y. S. Jung, *J. Power Sources*, 2015, **274**, 1254-1262.

[17] C. Fu, J. Wang, J. Wang, L. Meng, W. Zhang, X. Li and L. Li, *J. Mater. Chem. A*, 2019, **7**, 23149-23161.

[18] J. Li, L. Baggetto, S. K. Martha, G. M. Veith, J. Nanda, C. Liang and N. J. Dudney, *Adv. Energy Mater.*, 2013, **3**, 1275-1278.

[19] B. Xiao, J. Liu, Q. Sun, B. Wang, M. N. Banis, D. Zhao, Z. Wang, R. Li, X. Cui, T. K. Sham and X. Sun, *Adv. Sci.*, 2015, **2**, 1500022.

[20] D. W. Kim, S. Uchida, H. Shiiba, N. Zettsu and K. Teshima, *Sci. Rep.*, 2018, **8**, 11771-11780.

[21] H. Sun, B. Xia, W. Liu, G. Fang, J. Wu, H. Wang, R. Zhang, S. Kaneko, J. Zheng, H. Wang and D. Li, *Appl. Surf. Sci.*, 2015, **331**, 309-314.

[22] B. Chang, J. Kim, Y. Cho, I. Hwang, M. S. Jung, K. Char, K. T. Lee, K. J. Kim and J. W. Choi, *Adv. Energy Mater.*, 2020, **10**, 2001069.

[23] Y. Tang, J. Deng, W. Li, O. I. Malyi, Y. Zhang, X. Zhou, S. Pan, J. Wei, Y. Cai, Z. Chen and X. Chen, *Adv. Mater.*, 2017, **29**, 1701828.

[24] A. Tornheim, S. Sharifi-Asl, J. C. Garcia, J. Bareño, H. Iddir, R. Shahbazian-Yassar and Z. Zhang, *Nano Energy*, 2019, **55**, 216-225.

[25] D. Guy, B. Lestriez and D. Guyomard, *Adv. Mater.*, 2004, **16**, 553-557.

[26] D. Guy, B. Lestriez, R. Bouchet and D. Guyomard, *J. Electrochem. Soc.*, 2006, **153**, A679-A688.

[27] W.-Y. Chou, Y.-C. Jin, J.-G. Duh, C.-Z. Lu and S.-C. Liao, *Appl. Surf. Sci.*, 2015, **355**, 1272-1278.

[28] T. Dong, H. Zhang, Y. Ma, J. Zhang, X. Du, C. Lu, X. Shangguan, J. Li, M. Zhang, J. Yang, X. Zhou and G. Cui, *J. Mater. Chem. A*, 2019, **7**, 24594-24601.

[29] H. Isozumi, K. Kubota, R. Tatara, T. Horiba, K. Hida, T. Matsuyama, S. Yasuno and S. Komaba, *ACS Appl. Energy Mater.*, 2020, **3**, 7978-7987.

[30] H. Q. Pham, J. Lee, H. M. Jung and S.-W. Song, *Electrochim. Acta*, 2019, **317**, 711-721.

[31] W. Zeng, L. Wang, X. Peng, T. Liu, Y. Jiang, F. Qin, L. Hu, P. K. Chu, K. Huo and Y. Zhou, *Adv. Energy Mater.*, 2018, **8**, 1702314.

[32] S. Huang, J. Ren, R. Liu, Y. Bai, X. Li, Y. Huang, M. Yue, X. He and G. Yuan, *ACS Sustain. Chem. Eng.*, 2018, **6**, 12650-12657.

[33] Y. Qian, S. Hu, X. Zou, Z. Deng, Y. Xu, Z. Cao, Y. Kang, Y. Deng, Q. Shi, K. Xu and Y. Deng, *Energy Storage Mater.*, 2019, **20**, 208-215.

[34] L. Xue, K. Ueno, S.-Y. Lee and C. A. Angell, *J. Power Sources*, 2014, **262**, 123-128.

[35] H. J. Song, S. H. Jang, K. Choi, S. C. Nam, J. Mun and T. Yim, *ACS Sustain. Chem. Eng.*, 2020, **8**, 7316-7323.

[36] G. Xu, C. Pang, B. Chen, J. Ma, X. Wang, J. Chai, Q. Wang, W. An, X. Zhou, G. Cui and L. Chen, *Adv. Energy Mater.*, 2018, **8**, 1701398.

[37] J. Li, J. Wu, S. Li, G. Liu, Y. Cui, Z. Dong, H. Liu and X. Sun, *ChemSusChem*, 2021, **14**, 2721-2730.

[38] M.-H. Ryou, S. Hong, M. Winter, H. Lee and J. W. Choi, *J. Mater. Chem. A*, 2013, **1**, 15224-15229.

[39] F. Bigoni, F. De Giorgio, F. Soavi and C. Arbizzani, *J. Electrochem. Soc.*, 2017, **164**, A6171-A6177.

[40] L. Rao, X. Jiao, C. Y. Yu, A. Schmidt, C. O'Meara, J. Seidt, J. R. Sayre, Y. M. Khalifa and J. H. Kim, *ACS Appl. Mater. Interfaces*, 2022, **14**, 861-872.

[41] I. Kovalenko, B. Zdyrko, A. Magasinski, B. Hertzberg, Z. Milicev, R. Burtovyy, I. Luzinov and G. Yushin, *Science*, 2011, **334**, 75-79.

[42] Y. K. Jeong, T.-w. Kwon, I. Lee, T.-S. Kim, A. Coskun and J. W. Choi, *Energy Environ. Sci.*, 2015, **8**, 1224-1230.

[43] T. Zhang and R. E. Marchant, *J. Colloid & Interface Sci.*, 1996, **177**, 419-426.

[44] M. L. Coote, C. Y. Lin and A. A. Zavitsas, *Phys Chem Chem Phys*, 2014, **16**, 8686-8696.

[45] K. Jung, S. H. Oh and T. Yim, *J. Electrochem. Sci. Technol.*, 2021, **12**, 67-73.

[46] N. Xu, J. Shi, G. Liu, X. Yang, J. Zheng, Z. Zhang and Y. Yang, *J. Power Sources Adv.*, 2021, **7**, 100043-100058.

[47] J. Yang, I. Shkrob, K. Liu, J. Connell, N. L. Dietz Rago, Z. Zhang and C. Liao, *J. Electrochem. Soc.*, 2020, **167**, 070533-070540.

[48] L. Wang, H. Li, X. Huang and E. Baudrin, *Solid State Ionics*, 2011, **193**, 32-38.

[49] J. Yang, X. Han, X. Zhang, F. Cheng and J. Chen, *Nano Research*, 2013, **6**, 679-687.

[50] J. Zhang, G. Sun, Y. Han, F. Yu, X. Qin, G. Shao and Z. Wang, *Electrochim. Acta*, 2020, **343**, 136105-136114.

[51] C. Yin, H. Zhou, Z. Yang and J. Li, *ACS Appl. Mater. Interfaces*, 2018, **10**, 13625-13634.

[52] B. Philippe, R. Dedryvère, J. Allouche, F. Lindgren, M. Gorgoi, H. Rensmo, D. Gonbeau and K. Edström, *Chem. Mater.*, 2012, **24**, 1107-1115.

[53] X. Ren, L. Zou, S. Jiao, D. Mei, M. H. Engelhard, Q. Li, H. Lee, C. Niu, B. D. Adams, C. Wang, J. Liu, J.-G. Zhang and W. Xu, *ACS Energy Lett.*, 2019, **4**, 896-902.

[54] T. Deng, X. Fan, L. Cao, J. Chen, S. Hou, X. Ji, L. Chen, S. Li, X. Zhou, E. Hu, D. Su, X.-Q. Yang and C. Wang, *Joule*, 2019, **3**, 2550-2564.

[55] S. Lin, H. Hua, Z. Li and J. Zhao, *ACS Appl. Mater. Interfaces*, 2020, **12**, 33710-33718.

[56] W. Liu, P. Oh, X. Liu, M. J. Lee, W. Cho, S. Chae, Y. Kim and J. Cho, *Angew. Chem. Int. Ed.*, 2015, **54**, 4440-4457.

[57] C. Wang, Y. S. Meng and K. Xu, *J. Electrochem. Soc.*, 2018, **166**, A5184-A5186.

[58] X. Ren, L. Zou, X. Cao, M. H. Engelhard, W. Liu, S. D. Burton, H. Lee, C. Niu, B. E. Matthews, Z. Zhu, C. Wang, B. W. Arey, J. Xiao, J. Liu, J.-G. Zhang and W. Xu, *Joule*, 2019, **3**, 1662-1676.

[59] Y. Wu, D. Ren, X. Liu, G. L. Xu, X. Feng, Y. Zheng, Y. Li, M. Yang, Y. Peng, X. Han, L. Wang, Z. Chen, Y. Ren, L. Lu, X. He, J. Chen, K. Amine and M. Ouyang, *Adv. Energy Mater.*, 2021, **11**, 2102299.

[60] W. Li, A. Dolocan, P. Oh, H. Celio, S. Park, J. Cho and A. Manthiram, *Nat. Commun.*, 2017, **8**, 14589-14598.

[61] T. Sugimoto, Y. Atsumi, M. Kikuta, E. Ishiko, M. Kono and M. Ishikawa, *J. Power Sources*, 2009, **189**, 802-805.

[62] H. Zhang, C. Li, M. Piszcz, E. Coya, T. Rojo, L. M. Rodriguez-Martinez, M. Armand and Z. Zhou, *Chem. Soc. Rev.*, 2017, **46**, 797-815.

[63] H. Huo, B. Wu, T. Zhang, X. Zheng, L. Ge, T. Xu, X. Guo and X. Sun, *Energy Storage Mater.*, 2019, **18**, 59-67.

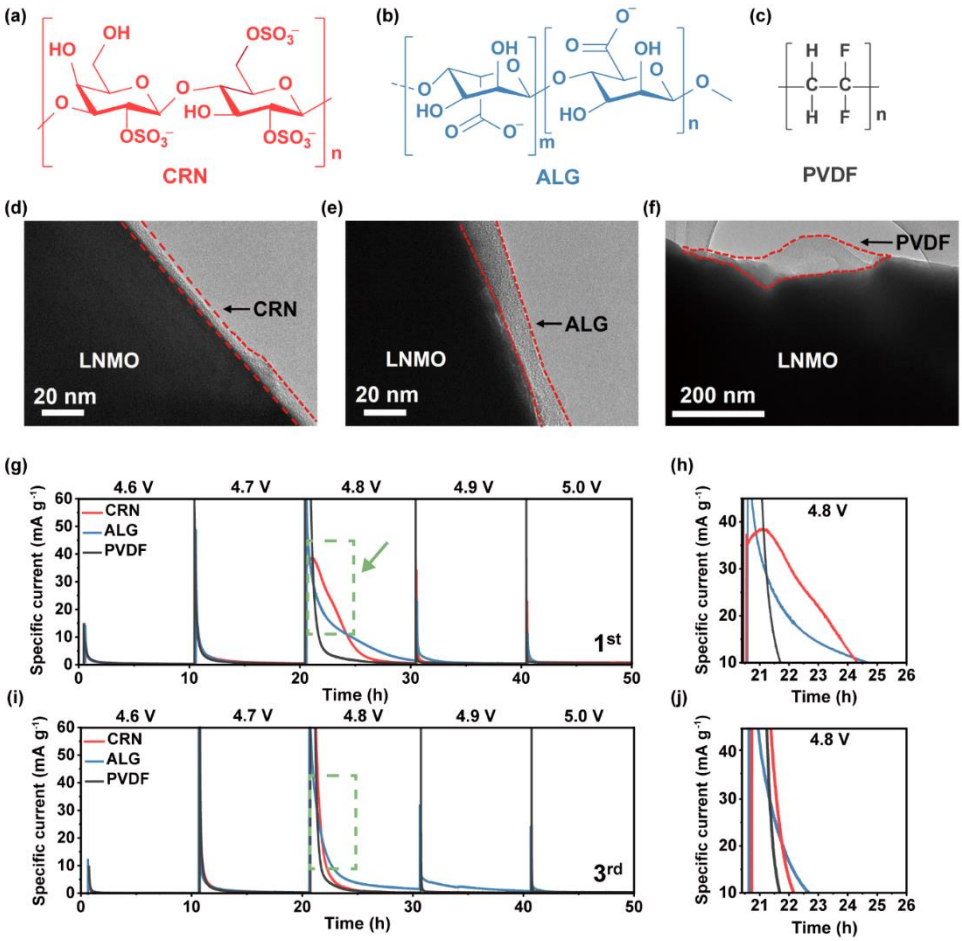

Figure 2.1. Physicochemical and electrochemical properties of the CRN, ALG, and PVDF polymeric binders. Chemical structures of (a) CRN, (b) ALG, and (c) PVDF. TEM images of (d) CRN, (e) ALG, and (f) PVDF on the LNMO surface in the pristine state. The red dashed lines indicate the surface regions covered by the binders. Electrochemical floating tests of the CRN-, ALG-, and PVDF-based electrodes at the (g and h) first and (i and j) third charging periods. (h and j) Enlargements of the areas demarcated by the green dashed lines in (g and i), respectively.

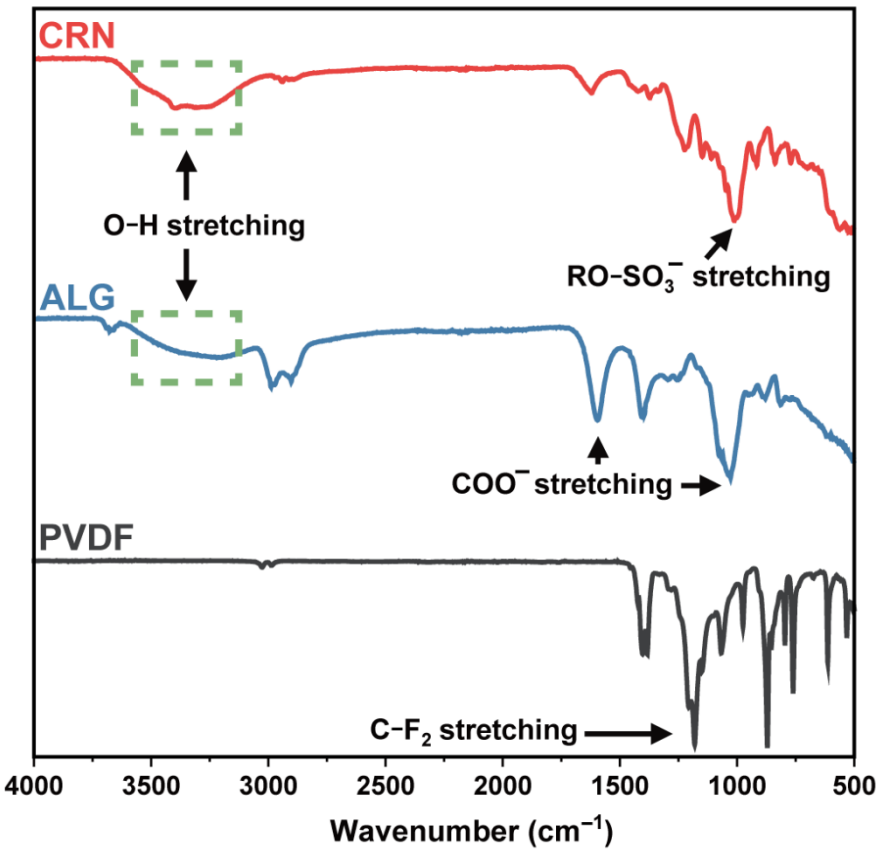

Figure 2.2. FT-IR spectra of the CRN, ALG, and PVDF polymeric binders. The appearances of broad O–H stretching bands at 3600–3200 cm^{-1} for both the CRN and ALG were detected. The stretching bands of the sulfate ($–OSO_3^-$) of the CRN at 1149–1015 cm^{-1}, the carboxylate ($–COO^-$) of the ALG at 1600 and 1127 cm^{-1}, and the carbon fluoride ($C–F_2$) of the PVDF at 1080 cm^{-1} were characterized.

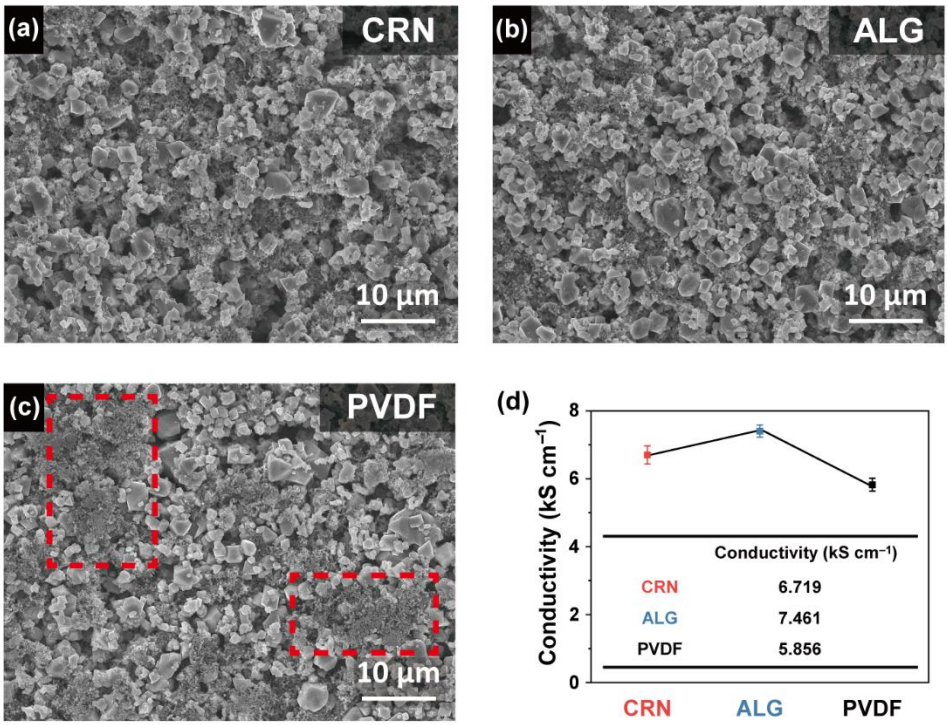

Figure 2.3. Top-view SEM images of the (a) CRN-, (b) ALG-, and (c) PVDF-based electrodes in the pristine state. The red dashed boxes in (c) indicate baling of the conducting agent. (d) Electronic conductivities of the electrodes from four-point probe measurements.

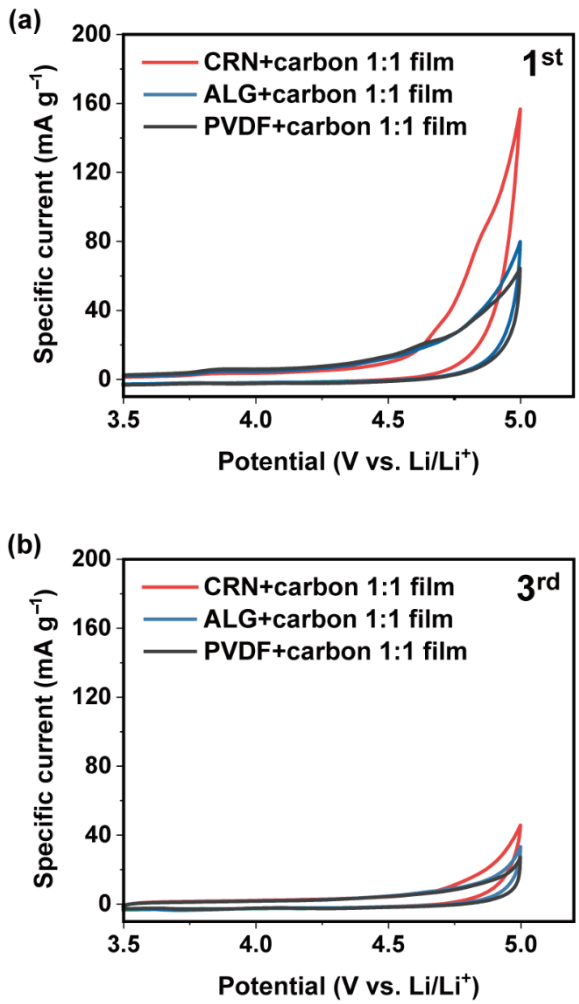

Figure 2.4. CV curves of the binder-conducting agent composite films (1:1, w/w) at the (a) first and (b) third cycles until 5.0 V (*vs.* Li/Li^+) at a scan rate of 0.05 mV s^{-1}.

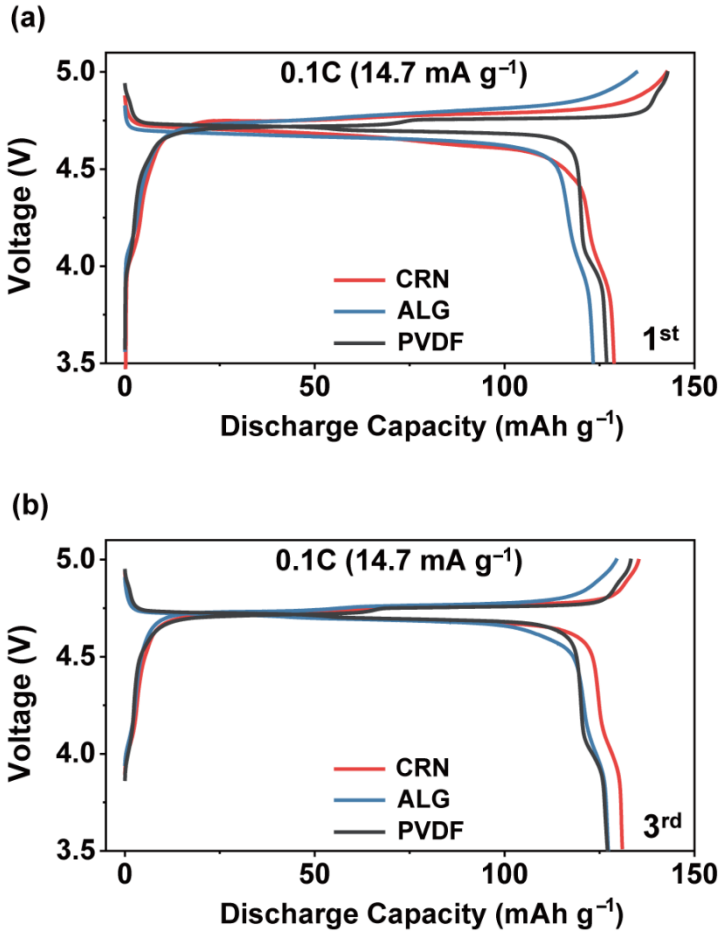

Figure 2.5. Voltage profiles of the CRN-, ALG-, and PVDF-based electrodes when measured at 0.1C in the (a) first and (b) third formation cycles.

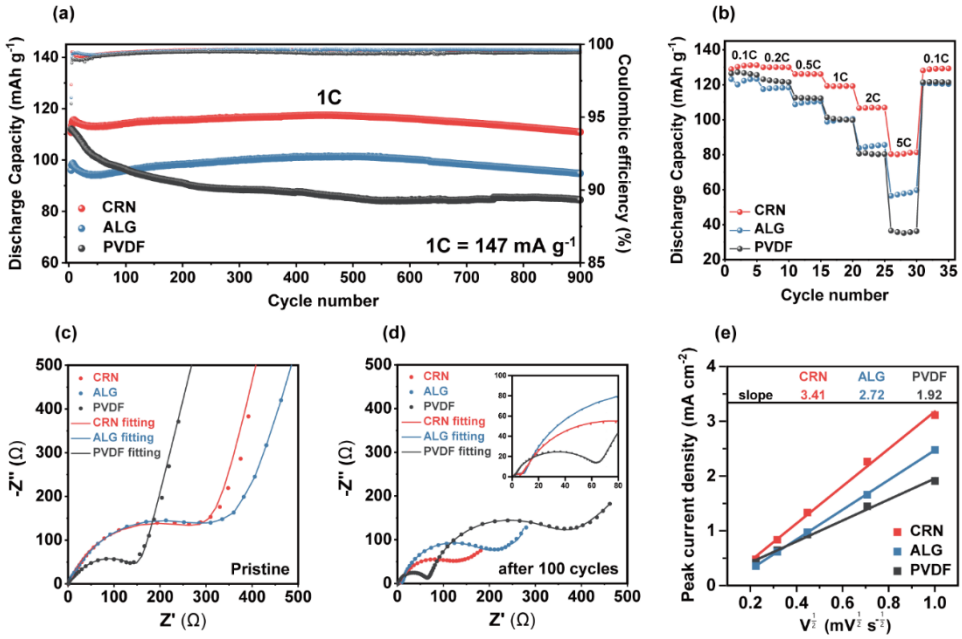

Figure 2.6. Electrochemical performance of the CRN-, ALG-, and PVDF-based electrodes. (a) Discharge capacities and CEs during 900 cycles when performed at 1C (147 mA g^{-1}) in the potential range of 3.5–5.0 V vs. Li/Li^+ after three formation cycles at 0.1C (14.7 mA g^{-1}) in the half-cell configuration. (b) Rate performance at different C-rates. Nyquist plots were fitted (c) in the pristine state and (d) after 100 cycles. (e) Relationship between the peak current (i_p) and square root of the scan rate ($v^{1/2}$) from CV data.

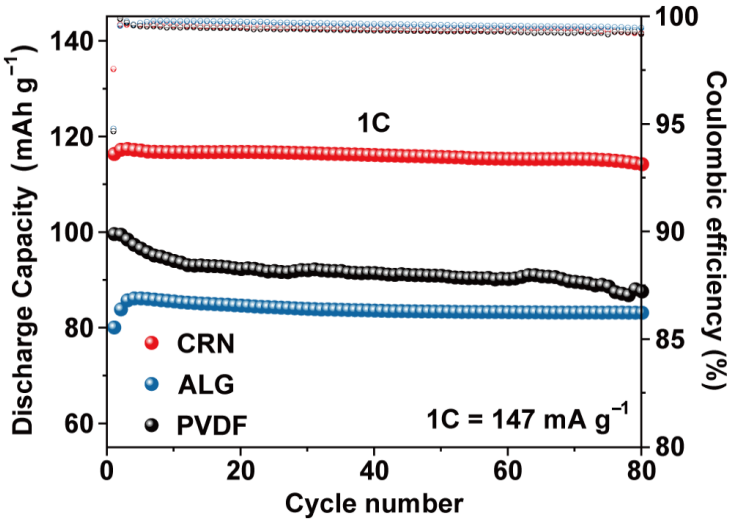

Figure 2.7. Discharge capacities and CEs of the CRN-, ALG-, and PVDF-based electrodes with a high loading of the active material (10 mg cm^{-2}) when cycled at 1C after three formation cycles.

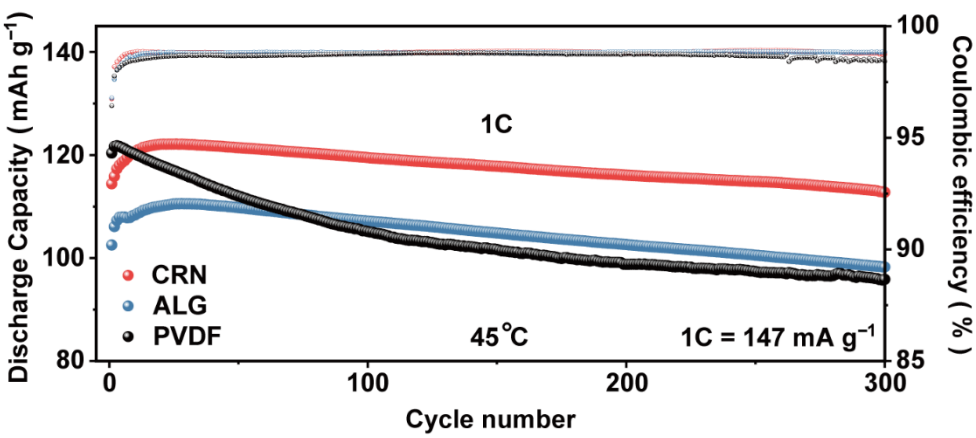

Figure 2.8. Discharge capacities and CEs of the CRN-, ALG-, and PVDF-based cells when measured at 1C during 300 cycles at 45 °C. Before cycling at 1C, the cells were operated for three formation cycles at 0.1C at 25 °C to induce a stable CEI layer.

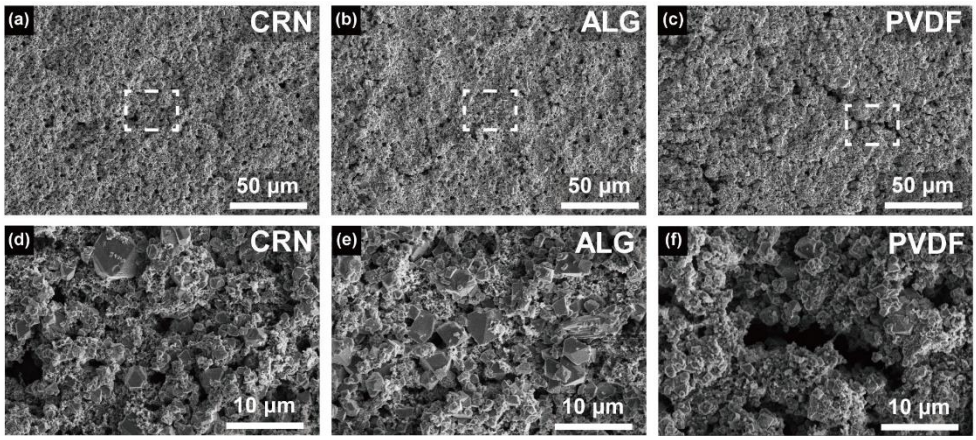

Figure 2.9. Top-view SEM images of the (a) CRN-, (b) ALG-, and (c) PVDF-based electrodes after 100 cycles. (d-f) Magnifications of the areas enclosed by the white dashed boxes in (a-c).

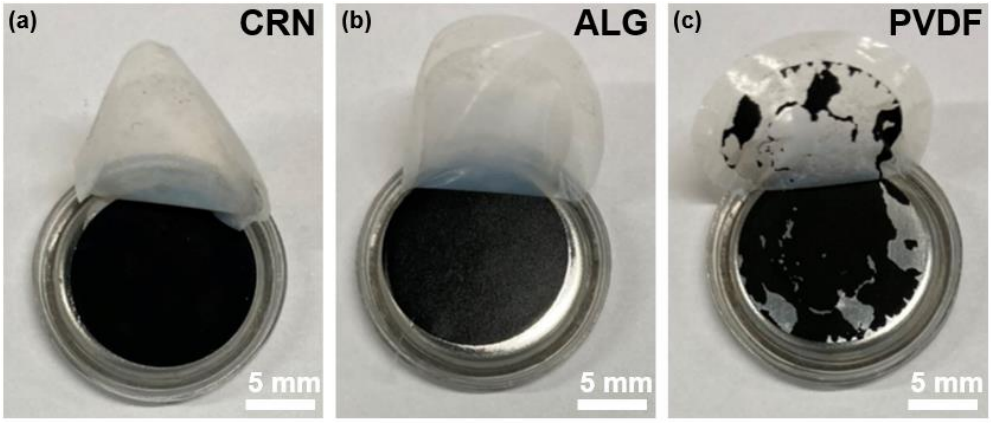

Figure 2.10. Digital images of the (a) CRN-, (b) ALG-, and (c) PVDF-based electrodes after 100 cycles.

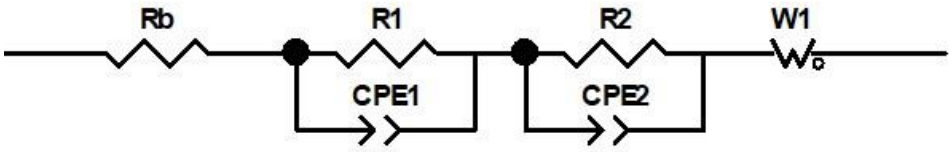

Figure 2.11. Equivalent circuit used for fitting the Nyquist plots of the CRN-, ALG-, and PVDF-based electrodes.

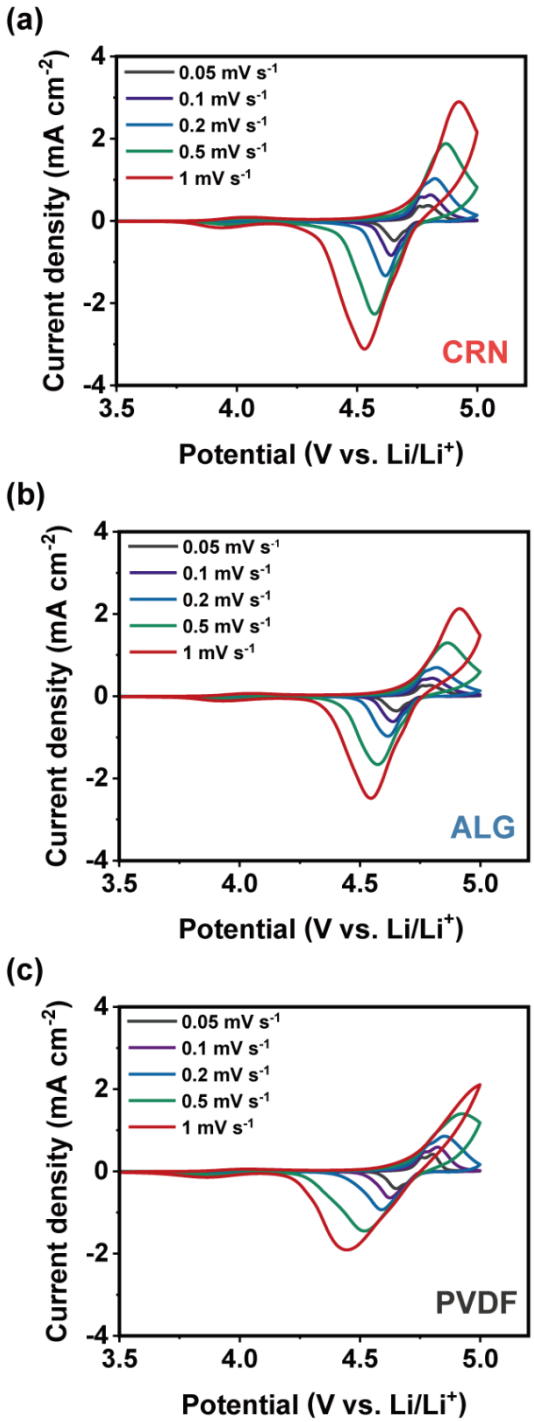

Figure 2.12. CV curves when measured at various scan rates from 0.05 to 1 mV s^{-1} of the (a) CRN-, (b) ALG-, and (c) PVDF-based electrodes.

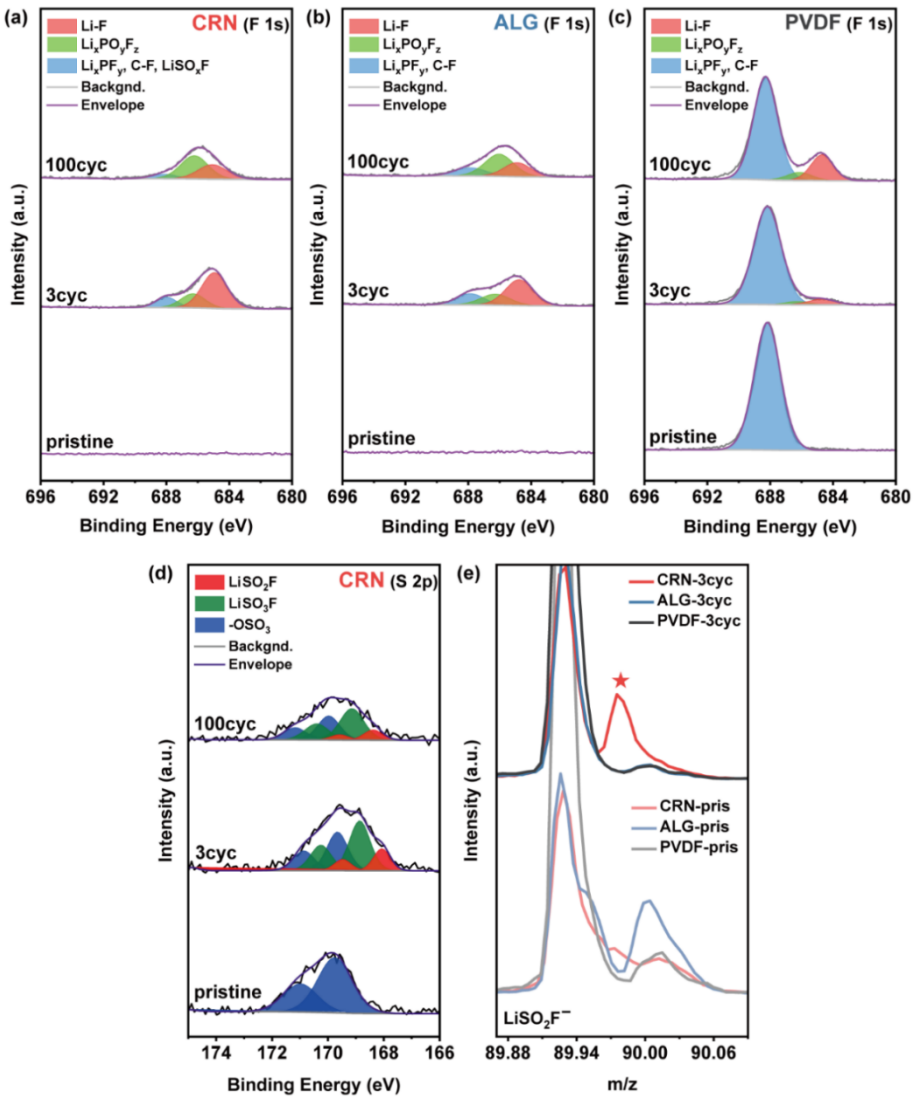

Figure 2.13. Identification of the CEI components in the CRN-, ALG-, and PVDF-based electrodes. F 1s XPS results of the (a) CRN-, (b) ALG-, and (c) PVDF-based electrodes in the pristine state, after three formation cycles at 0.1C, and after 100 cycles at 1C. (d) S 2p XPS results of the CRN-based electrode in the pristine state, after three formation cycles at 0.1C, and after 100 cycles at 1C. (e) ToF-SIMS mass spectra of $LiSO_2F^-$ secondary ion fragments for the three binder-based electrodes in the pristine state and after three formation cycles at 0.1C. The asterisk-marked peak represents the m/z eigenvalue of the $LiSO_2F^-$ ion fragments (Li = 7.016, S = 31.972, O = 15.994, and F = 18.998).

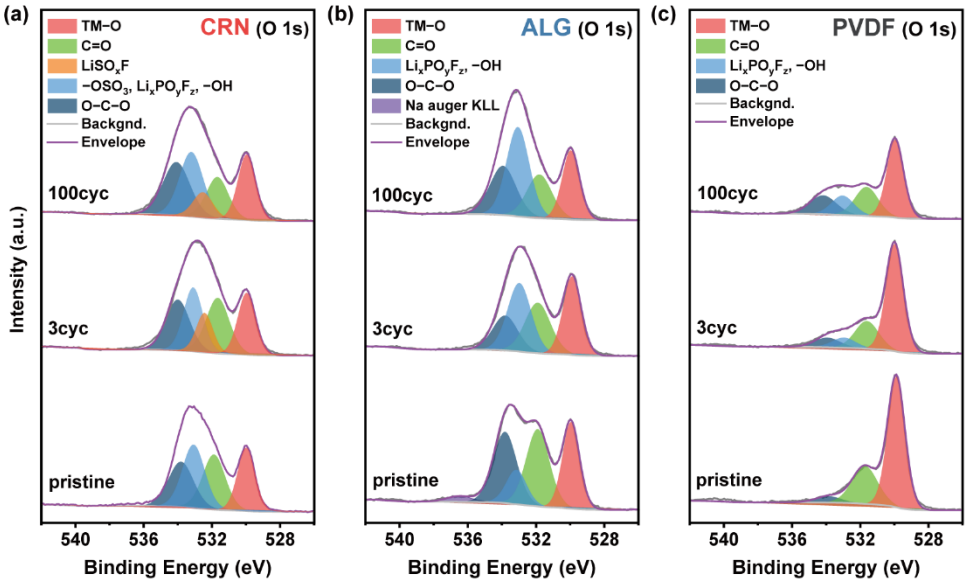

Figure 2.14. O 1s XPS profiles of the (a) CRN-, (b) ALG-, and (c) PVDF-based electrodes in the pristine state, after three formation cycles at 0.1C, and after 100 cycles at 1C.

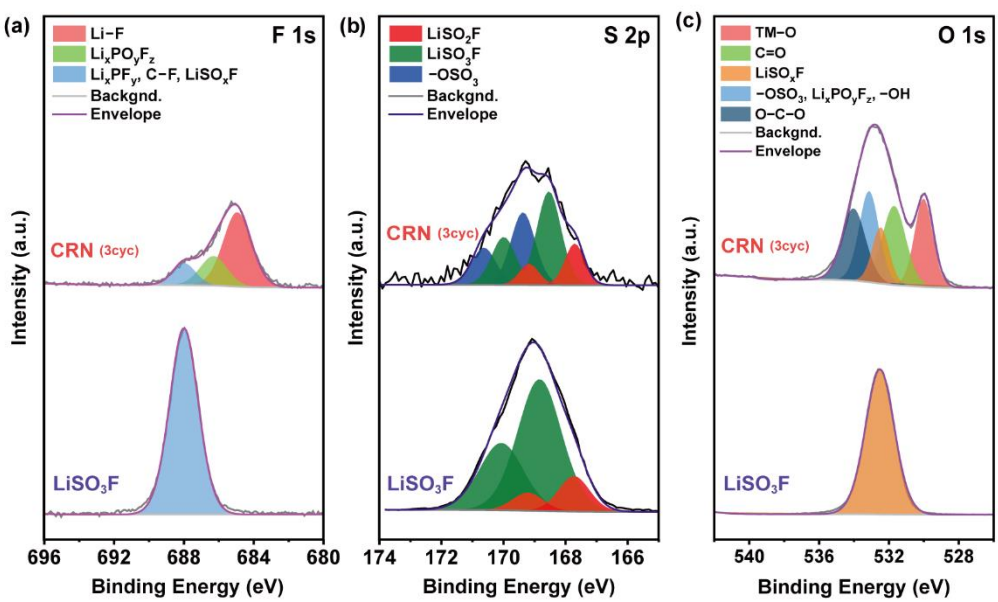

Figure 2.15. XPS profiles of the commercial $LiSO_3F$ and CRN-based electrode after three formation cycles at 0.1C: (a) F 1s, (b) S 2p, and (c) O 1s spectra.

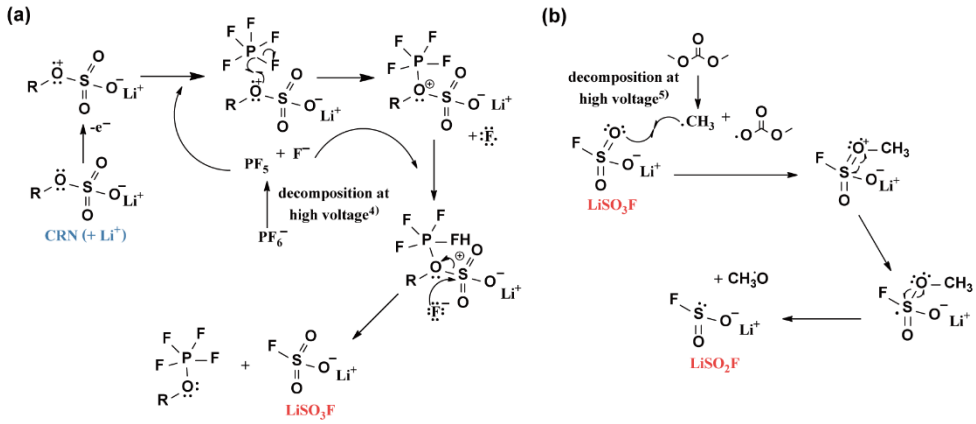

Figure 2.16. Suggested mechanism of the electrochemical formation of (a) $LiSO_3F$ and (b) $LiSO_2F$ in the CRN-based electrode. The sulfate moieties in the CRN are oxidized at high voltage, followed by a radical reaction with the Lewis acidic PF_5 from $LiPF_6$. The fluoride ion attacks the sulfur atom of the intermediate complex and eventually forms $LiSO_3F$. $LiSO_3F$ further reacts with decomposed organic radicals from the carbonate molecule and transforms into $LiSO_2F$ by losing oxygen.

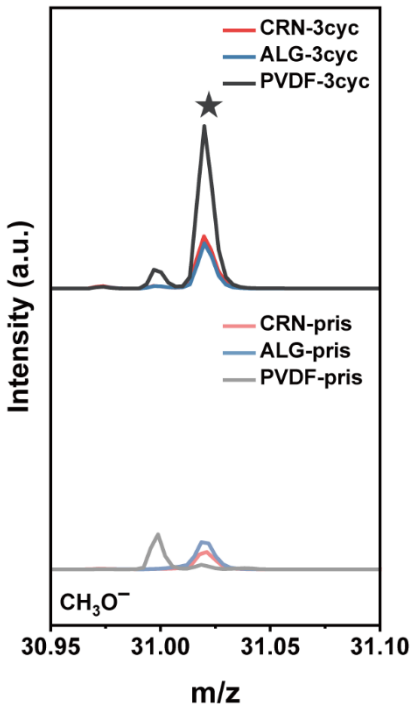

Figure 2.17. ToF-SIMS results of CH_3O^- secondary ion fragments of the CRN-, ALG-, and PVDF-based electrodes in the pristine state and after three formation cycles. The asterisk represents the m/z eigenvalue of the CH_3O^- ion fragment (C = 12.000, H = 1.008, and O = 15.994).

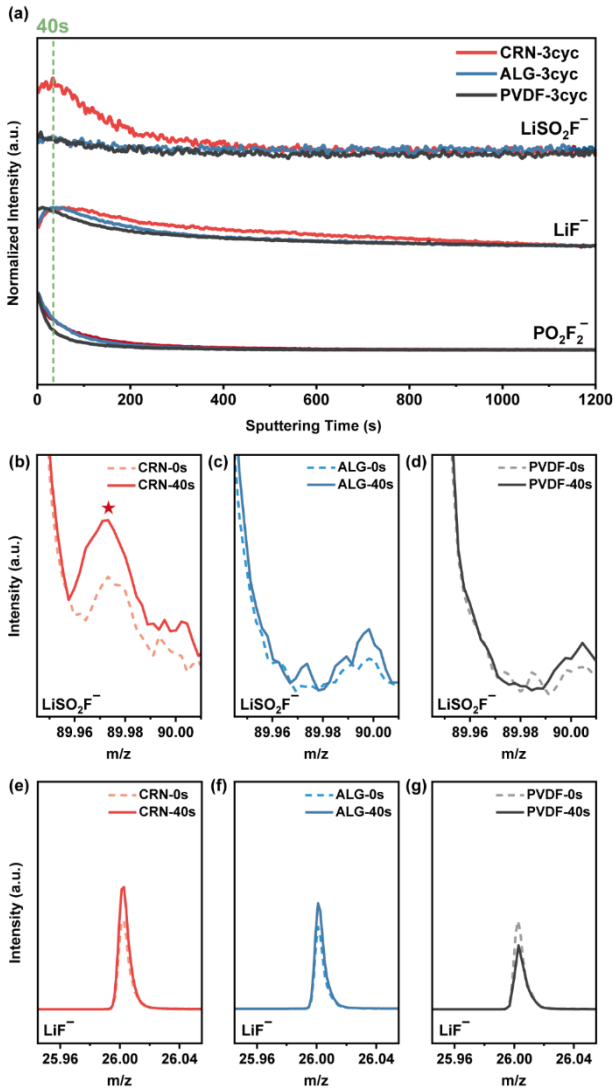

Figure 2.18. Different locations of inorganic CEI components in the CRN-, ALG-, and PVDF-based electrodes. (a) ToF-SIMS depth profiles of $LiSO_2F^-$, LiF^-, and $PO_2F_2^-$ secondary ion fragments for the three binder-based electrodes after three formation cycles at 0.1C. ToF-SIMS mass spectra were generated *via* the reconstruction function from the depth profile data. ToF-SIMS mass spectra of $LiSO_2F^-$ secondary ion fragment in the (b) CRN-, (c) ALG-, and (d) PVDF-based electrodes at sputtering times of 0 and 40 seconds. ToF-SIMS mass spectra of LiF^- secondary ion fragment in the (e) CRN-, (f) ALG-, and (g) PVDF-based electrodes at sputtering times of 0 and 40 seconds.

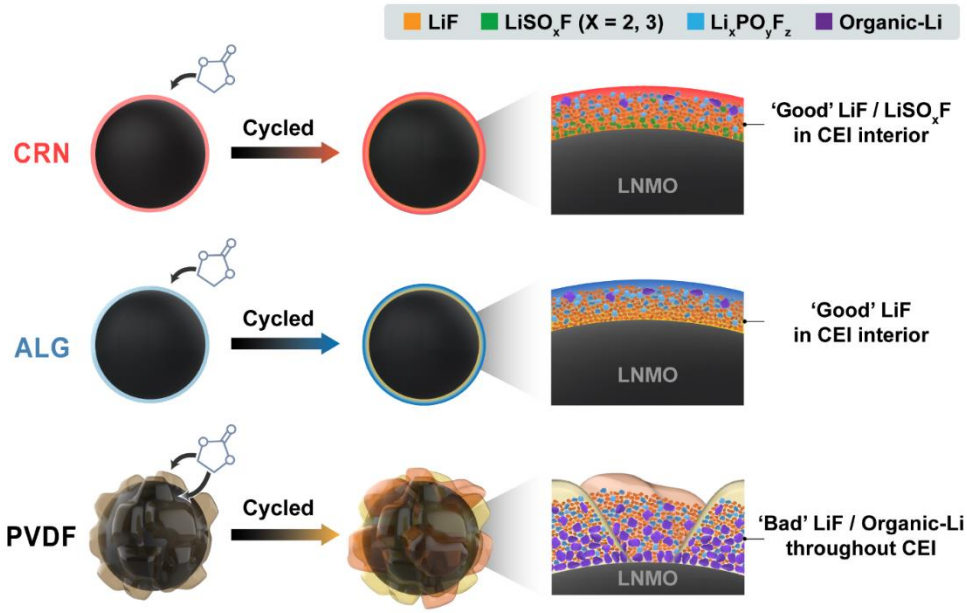

Figure 2.19. Schematic illustrations of the CEI formation of PVDF-, ALG-, and CRN-based electrodes.

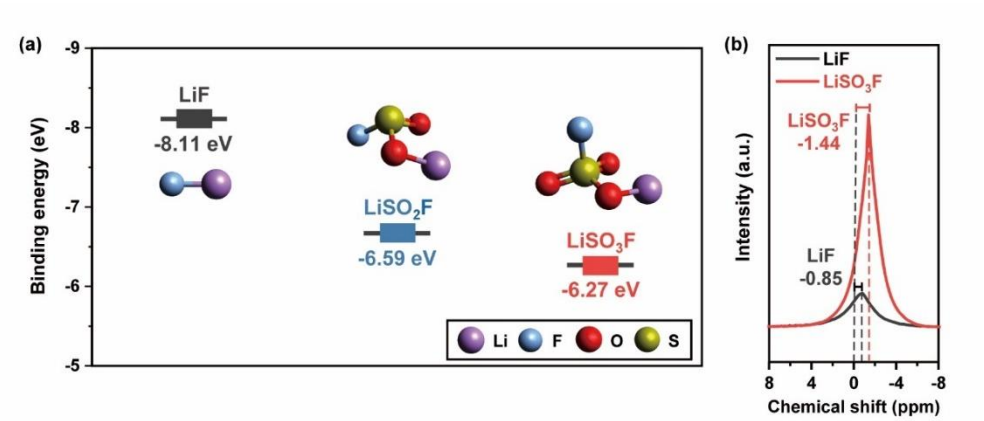

Figure 2.20. Li ion binding affinity of LiF and LiSO$_x$F (x = 2, 3) CEI components. (a) Li ion binding energy of LiF and LiSO$_x$F (x = 2, 3) *via* DFT calculation using the GAUSSIAN16 software package. (b) ^{7}Li MAS NMR spectra of LiF and LiSO$_3$F.

Sample	Pristine	after 100 cycles	
	R_{CT} (Ω)	R_{CEI} (Ω)	R_{CT} (Ω)
CRN	305.0	4.5	88.9
ALG	343.1	7.2	155.1
PVDF	139.5	64.2	252.9

Table 2.1. R_{CEI} and R_{CT} values of the three electrodes in the pristine state and after 100 cycles.

국문초록

21세기에 접어들면서 지구온난화가 가속화됨에 따라, 지속 가능한 발전을 위해 탄소 배출에 대한 규제 방안이 활발하게 논의되고 있다. 이에 대한 일환으로 전기자동차의 상용화가 본격적으로 시작되면서 리튬이차전지 및 차세대전지에 대한 관심이 급증하고 있다. 현재, 주행거리 향상을 목표로 전극의 에너지밀도를 증가시키기 위해 연구가 진행되고 있는데, 양극 파트에서는 층상계, 스피넬 구조 등의 고전압 양극재가 요구되는 수요를 충족할 유력한 후보로 여겨진다.

하지만, 해당 양극재를 높은 cut-off voltage 조건에서 구동하면 양극-전해질 계면이 매우 불안정해져 전해질 분해 등의 표면 열화가 발생한다. 이를 해결하기 위한 다양한 시도가 존재하나, 본 연구에서는 주로 전극 구성물질 간의 접착제로서의 역할만을 고수해왔던 바인더에 고분자 구조 및 작용기의 다각적 설계를 통해 고전압 양극재의 계면 안정화 기능을 새로이 부여하고자 하였다. 기존 상용화된 PVDF 바인더는 양극재의 metal oxide와는 비교적 약한 van der Waals interaction을 기반으로 결합한다. 따라서, 양극재 표면에 대한 coverage가 부족하여 naïve한 양극재 표면을 전해질에 많이 노출시킨다. 하지만, 본 연구에서는 양극재의 metal oxide와의 hydrogen bonding, ion-dipole interaction 등의 강한 interaction을 기반으로 우수한 coverage를 유도할 수 있는 바인더를 개발하여 각종 표면 부반응을 완화하고 안정적인 CEI를 형성할 수 있도록 시도하였다.

주요어 : 균일한 도포, 표면 열화, 양극-전해질 계면, 고분자 바인더, 고전압 양극재, 리튬이온전지

학 번 : 2018-35512